NAVAL POSTGRADUATE SCHOOL

MONTEREY, CALIFORNIA

THESIS

REFLECTION AND BRAGG SCATTERING ALONG ROCKY SHORES

by

Patrick Collins

March 2023

Thesis Advisor:	James H. MacMahan
Second Reader:	Edward B. Thornton

THIS PAGE INTENTIONALLY LEFT BLANK

REPORT DOCUMENTATION PAGE			*Form Approved OMB No. 0704-0188*

1. AGENCY USE ONLY ***(Leave blank)***	**2. REPORT DATE** March 2023	**3. REPORT TYPE AND DATES COVERED** Master's thesis

4. TITLE AND SUBTITLE REFLECTION AND BRAGG SCATTERING ALONG ROCKY SHORES	**5. FUNDING NUMBERS**
6. AUTHOR(S) Patrick Collins	
7. PERFORMING ORGANIZATION NAME(S) AND ADDRESS(ES) Naval Postgraduate School Monterey, CA 93943-5000	**8. PERFORMING ORGANIZATION REPORT NUMBER**
9. SPONSORING / MONITORING AGENCY NAME(S) AND ADDRESS(ES) N/A	**10. SPONSORING / MONITORING AGENCY REPORT NUMBER**

11. SUPPLEMENTARY NOTES The views expressed in this thesis are those of the author and do not reflect the official policy or position of the Department of Defense or the U.S. Government.

12a. DISTRIBUTION / AVAILABILITY STATEMENT Approved for public release. Distribution is unlimited.	**12b. DISTRIBUTION CODE** A

13. ABSTRACT (maximum 200 words)

Field observations of shoreline reflection and Bragg scattering for sea and swell waves along varying rocky shores from Monterey to Santa Cruz, CA, are described in comparison to sandy shores. The estimates are derived from directional spectra obtained primarily from Global Positioning System (GPS)-based Spotter wave-buoys. Wave reflection and Bragg scattering vary by shoreline type, with sandy shores reflecting up to 23% and rocky shores reflecting up to 30% at rocky platforms. However, rocky shores with cliffs reflected up to 14% and rough rocky shores up to 8%. A new estimator is proposed that accounts for the decrease in reflection for rocky shores associated with increasing shoreline roughness and works well for both rocky and sandy shores (r^2=0.45). Bragg scattering was expected along rocky shores due to the large bottom roughness and scales that coincide with the resonant response for sea and swell waves. However, the absence of Bragg scattering is believed to be associated with the non-uniformity of the bottom roughness and moderate bottom profile slope, which leads to an insufficient number of wave-bottom interactions for development. The directional narrowing with decreasing water depth is similar to sandy shores. The study describes aspects of sea swell transformation that occurs for rocky shores with observations and theory.

14. SUBJECT TERMS rocky shores, Bragg scattering, reflection, directional spectrum, buoy observations, in situ oceanic observations;	**15. NUMBER OF PAGES** 65
	16. PRICE CODE

17. SECURITY CLASSIFICATION OF REPORT Unclassified	**18. SECURITY CLASSIFICATION OF THIS PAGE** Unclassified	**19. SECURITY CLASSIFICATION OF ABSTRACT** Unclassified	**20. LIMITATION OF ABSTRACT** UU

NSN 7540-01-280-5500

Standard Form 298 (Rev. 2-89)
Prescribed by ANSI Std. 239-18

THIS PAGE INTENTIONALLY LEFT BLANK

Approved for public release. Distribution is unlimited.

REFLECTION AND BRAGG SCATTERING ALONG ROCKY SHORES

Patrick Collins
Lieutenant, Royal Australian Navy
BS, University of New South Wales, 2012

Submitted in partial fulfillment of the
requirements for the degree of

MASTER OF SCIENCE IN PHYSICAL OCEANOGRAPHY

from the

NAVAL POSTGRADUATE SCHOOL
March 2023

Approved by: James H. MacMahan
Advisor

Edward B. Thornton
Second Reader

Peter C. Chu
Chair, Department of Oceanography

THIS PAGE INTENTIONALLY LEFT BLANK

ABSTRACT

Field observations of shoreline reflection and Bragg scattering for sea and swell waves along varying rocky shores from Monterey to Santa Cruz, CA, are described in comparison to sandy shores. The estimates are derived from directional spectra obtained primarily from Global Positioning System (GPS)-based Spotter wave-buoys. Wave reflection and Bragg scattering vary by shoreline type, with sandy shores reflecting up to 23% and rocky shores reflecting up to 30% at rocky platforms. However, rocky shores with cliffs reflected up to 14% and rough rocky shores up to 8%. A new estimator is proposed that accounts for the decrease in reflection for rocky shores associated with increasing shoreline roughness and works well for both rocky and sandy shores (r^2=0.45). Bragg scattering was expected along rocky shores due to the large bottom roughness and scales that coincide with the resonant response for sea and swell waves. However, the absence of Bragg scattering is believed to be associated with the non-uniformity of the bottom roughness and moderate bottom profile slope, which leads to an insufficient number of wave-bottom interactions for development. The directional narrowing with decreasing water depth is similar to sandy shores. The study describes aspects of sea swell transformation that occurs for rocky shores with observations and theory.

THIS PAGE INTENTIONALLY LEFT BLANK

Table of Contents

THIS PAGE INTENTIONALLY LEFT BLANK

List of Figures

THIS PAGE INTENTIONALLY LEFT BLANK

List of Tables

THIS PAGE INTENTIONALLY LEFT BLANK

List of Acronyms and Abbreviations

ADCP	acoustic Doppler current profiler
AHRS	attitude and heading reference system
AS	Asilomar (experiment site)
BDM	Bayesian directional method
BS	Bragg scattering
CR	China Rock (experiment site)
CoNED	coastal national elevation database
EMEM	extended maximum entropy method
GPS	global positioning system
MAR	Marina (experiment site)
MC	Mitchell's Cove (experiment site)
NSC	North Sand City (experiment site)
PP	Pescadero Point (experiment site)
SC	Sand City (experiment site)
SCP	South Cypress Point (experiment site)
SIG1000	Nortek Signature 1000 (1MHz) ADCP
SS	sea-swell
TBDEM	topobathymetric digital elevation model
WAFO	wave analysis for fatigue and oceanography
WR	Wilder Ranch (experiment site)

THIS PAGE INTENTIONALLY LEFT BLANK

Acknowledgments

I extend my sincere gratitude to my advisor, Dr. Jamie MacMahan, for providing me with invaluable guidance and encouragement throughout my academic journey. Your unwavering support, exceptional mentorship, and genuine interest in my development as a scientist have been instrumental in shaping the trajectory of my research.

I would also like to express my appreciation to Dr. Ed Thornton, the reviewer of this thesis. Your insightful comments and feedback have helped refine this research and have significantly contributed to the quality of this thesis.

Furthermore, I wish to acknowledge the warm welcome and support that I received from my colleagues and new friends while studying abroad. Their encouragement and assistance have been invaluable in helping me to navigate this new academic environment. I extend my special thanks to Charlotte Benbow and Paul Jessen for their expertise in the field.

THIS PAGE INTENTIONALLY LEFT BLANK

CHAPTER 1:
Introduction

The significance of wave energy reflection by the shoreline and nearshore bottom-induced Bragg scattering for rocky shores is unknown for sea-swell (SS) band waves ($f = 0.04 - 0.2$ Hz). Field observations for sandy shores show that shoreline wave reflection can be significant (~20%), particularly for steeper beach slopes (Elgar et al. 1994). Bragg scattering by bottom undulations, such as bedforms (Ardhuin et al. 2003) and nearshore sandbars (Elgar et al. 2003), contribute toward larger reflection and increased directional spreading. Rocky shores support large bathymetric gradients with steep shoreline slopes and large amplitude (1 – 10 m) subaqueous bottom variability (Gon et al. 2020) with varying cross- and alongshore length scales where shoreline reflection and Bragg scattering are expected to co-occur. Nearshore directional wave observations along varying rocky shores near Monterey and Santa Cruz, California, USA, are used to examine the magnitude of SS wave energy reflection and Bragg scattering and are compared to sandy beaches.

Wave energy reflection, $R^2(f)$ is the ratio of offshore propagating energy, E_{off}, to onshore propagating energy, E_{on}, (Elgar et al. 1994) expressed as a function of frequency, f:

$$R^2(f) = \frac{E_{off}(f)}{E_{on}(f)} = \frac{\int_{90}^{270} S(f,\theta)\, d\theta}{\int_{-90}^{90} S(f,\theta)\, d\theta}, \tag{1.1}$$

with θ the angle relative to shore normal, and $S(f,\theta)$ is the directional spectrum. Bulk reflection in the SS band, $\overline{R^2}$ is calculated by energy-weighted $R^2(f)$ over the SS frequency band:

$$\overline{R^2} = \frac{\int^{SS} R^2(f) \cdot E(f)\, df}{\int^{SS} E(f)\, df}, \tag{1.2}$$

where $E(f)$ is the energy density spectrum of the surface elevation. Field observations from a natural sandy beach (Elgar et al. 1994) show that $\overline{R^2}$ was qualitatively consistent with the Miche number, M (Miche 1951), which was empirically derived for normally-incident,

monochromatic waves. M approximates R^2 and is given by:

$$R^2(f) \approx M = \frac{16g^2}{(2\pi)^5} \frac{\tan^5 \beta}{H_\infty^2 f^4}, \tag{1.3}$$

where g is gravity, β is the beach slope, H_∞ is the deep-water significant wave height, and f is the wave frequency. Based on Equation 1.3, $\overline{R^2}$ will increase with steepening β, decreasing f, and decreasing H_∞. For Duck, NC, $\overline{R^2}$ was as large as 0.18 and proportionally varied with β^5, where β tidally varied from 0.051 to 0.142 (Elgar et al. 1994). Other sandy beach observations show a similar reflection relationship with f and H_∞ (Huntley et al. 1999; Tatavarti et al. 1988; Walton 1992).

Bragg scattering is a phenomenon that happens when the wavelength of surface waves is twice the size of seafloor features, such as bedforms, that are oriented in the same direction as the waves (Elgar et al. 2003). Bragg scattering was observed by Elgar et al. (2003) on a sandy shore where there were a series of shore-parallel sinusoidal sandbars with a wavelength of approximately 50 m. As a result of this configuration, surface waves with a wavelength of around 100 m were scattered backward. This increased $\overline{R^2}$ from 0.4 at a nearby region without the sandbars to 0.7 where the sandbars were present.

When waves propagate at an angle φ to the bottom undulations, the wavelength of the surface wave must be longer by a factor of $1/\cos 2\varphi$ compared to the case where the waves propagate parallel to the bottom features. This Bragg condition is stated more generally in Ardhuin and Herbers (2002) in terms of wavenumbers. An incoming surface wave with wavenumber $\vec{k'}$ will resonantly interact with the bottom roughness wavenumber $\vec{l}$ to excite a surface (Bragg) wavenumber of $\vec{k} = \vec{k'} + \vec{l}$. As the frequency of the incoming and scattered waves are the same, so too is the magnitude of their wavenumbers, $|\vec{k'}| = |\vec{k}|$. This means that $\vec{l}$ must lie on $(0, 2|\vec{k'}|)$ if there is to be any Bragg scattering. The growth of Bragg waves can be calculated using the energy balance equation (Ardhuin and Herbers 2002). The transfer of energy $S_{Bragg}(\vec{k})$ for a given wavenumber $\vec{k}$ is defined by

$$S_{Bragg}(\vec{k}) = 4\pi g^{1/2} h^{-9/2} \chi(kh) \int_0^{2\pi} \cos^2(\theta - \theta') F^B(\vec{k} - \vec{k'}) \left[E(\vec{k'}) - E(\vec{k}) \right] d\theta', \tag{1.4}$$

with

$$\chi(kh) = \frac{(kh)^{9/2}\sqrt{\tanh(kh)}}{\sinh(2kh)\,[2kh + \sinh(2kh)]},$$

where h is water depth, F^B is the bottom elevation spectrum, $E(\vec{k'})$ is the energy at the incoming wavenumber, $E(\vec{k})$ is the energy at the Bragg wavenumber, and θ and θ' denote the direction associated with each respective surface wavenumber. Owing to the Bragg condition, the angle between the scattered and incident waves, $\theta - \theta'$, is twice the angle between the bottom undulations and the incident wave, $\theta - \theta' = 2\varphi$. Holding all other terms constant in Equation 1.4, the source term is largest when $\varphi = 0$ or 90°, and reduces to 0 as $\varphi \rightarrow 45°$. For each φ there is one acute combination of $\theta - \theta'$ and one obtuse. If $\theta - \theta'$ is acute, the resultant scattering is forward, and if $\theta - \theta'$ is obtuse, the scattering is backward. Owing to the Bragg condition, forward scattering will occur if $\sqrt{2}|\vec{k'}| > |\vec{l}|$ and backward scattering will occur if $\sqrt{2}|\vec{k'}| < |\vec{l}|$. Backward scattering would be observed by an increase in reflection (Elgar et al. 2003), and forward scattering would be observed as an increase in the directional spread of the incoming wave (Ardhuin et al. 2003).

According to Bird (2011), about 75 percent of the world's shorelines are categorized as rocky. These rocky shorelines can be classified as either rough, rocky shores or rocky platforms (Gon et al. 2020). Rocky platforms represent approximately 20 percent of all rocky shorelines, and they are nearly flat with a bottom roughness of 0.03 meters. The platforms are made up of erodible rock, which can result in offshore steps and a steep intertidal cliff (Kennedy and Beban 2005; Marshall and Stephenson 2011; Sunamura 1992; Poate et al. 2018). In contrast, rough, rocky shores have larger bottom roughness (greater than 1 meter) that extends from above the intertidal zone to the subtidal zone well offshore (Gon et al. 2020). The value of β scales with grain size based on the angle of repose (Bascom 1951; Dean and Dalrymple 1991; Reniers et al. 2013), is similar or larger at rocky shores than at sandy beaches. Therefore, based on Equation 1.3, $\overline{R^2}$ at rocky shores is expected to be the same or larger than that observed at sandy beaches. Interestingly, both coral reef studies and one rocky shore study found $\overline{R^2}$ to be small (less than 0.1) (Monismith et al. 2015; Gon et al. 2020). Observations of $\overline{R^2}$ for an artificial breakwater protecting Monterey Harbor, built from large (approximately 1 m) rocks with a slope of 0.6, ranged from 0.2 to 0.5, with variability primarily attributed to the dependence of $\overline{R^2}$ on $\overline{f}$ (Dickson et al. 1995). However, due to the limited number of observations for rocky shores, more field studies are

needed to fully understand wave reflection in this environment.

The bottom slope and elevation spectra computed from bathymetry (discussed further in section 2.1) off China Rock, Monterey, CA are compared to the bottom slope and elevation spectra off Cape Cod, MA and Duck, NC, where Bragg scattering was directly observed (Elgar et al. 2003) and inferred from observations (Ardhuin et al. 2003). The relative bottom slope and elevation variance at all wavenumbers are significantly larger at China Rocky (Figure 1.1a-b). The cross-shore bottom elevation and slope spectra at Cape Cod, MA, have distinct peaks at a wavenumber of 0.02 m^{-1} (Figure 1.1 b). The larger variance in bottom slope and elevation at China Rock suggest Bragg scattering should occur so long as the incoming waves are of the requisite geometry. For a given bottom elevation spectrum, the maximum of the source term in Equation 1.4 is calculated by assuming there is no energy at the scattered wavenumber, and the geometry is such that the incoming waves and scattered waves are parallel (e.g., the situation in Elgar et al. (2003)). This yields the following approximation for the maximum of the Bragg source term:

$$\max\left(S_{Bragg}(\vec{k})\right) \approx 4\pi g^{1/2} h^{-9/2} \chi(kh) F^B(2k), \tag{1.5}$$

$\max\left(S_{Bragg}\right)$ for the h and bottom wavenumber range at China Rock were calculated and shows the expected trend of $\max\left(S_{Bragg}\right)$ increasing as h decreases. In addition, as h decreases, the bottom wavenumber associated with the largest $\max\left(S_{Bragg}\right)$ changes, starting at $k \approx 10^{-2}$ m for $h = 30$m, increasing to $k \approx 2 \times 10^{-2}$ m when $h = 20$m (Figure 1.1c). This behavior is explained by the $\max\left(S_{Bragg}\right)$ dependence on F^B. The wavenumber of a surface gravity wave will vary with h owing to the linear wave dispersion relation:

$$\omega^2 = gk \tanh(kh) \tag{1.6}$$

where ω is the radian frequency, $\omega = 2\pi f$. By considering the dispersion relation and $\max\left(S_{Bragg}\right)$, the f of surface waves which satisfy the resonance condition with $\vec{l}$ that supports a large $\max\left(S_{Bragg}\right)$ for a given h is determined. A cross-shore spatial pattern emerges between f and expected Bragg scattering. Bragg scattering in the swell band ($0.05 < f < 0.125$ Hz) is expected to be 1 - 2 orders of magnitude larger than in the sea band ($0.125 < f < 0.3$ Hz) for $10 < h < 30$ m. For $h < 10$ m, both sea and swell band waves increase in Bragg scattering strength, and the frequency dependence becomes less

apparent (Figure 1.1c). Based on the average surface spectrum measured at China Rocky, energy throughout the SS band with a peak at $k = 8 \times 10^{-3}$ m^{-1} (Figure 1.1d). From the discussion above on Bragg scattering, the maximum backward Bragg scattering occurs when the bottom wavenumber is twice the surface wavenumber, mean energy spectra are given in terms of k and $2k$ in Figure 1.1d to show that the surface spectra coincide with the bottom spectra. The bottom elevation spectrum, the Bragg source, the bathymetry, and the average wave spectrum at China Rock suggest that Bragg scattering occurs at China Rock, and be more pronounced for lower frequencies in deeper water, then becomes spectrally uniform for depths shallower than 10m.

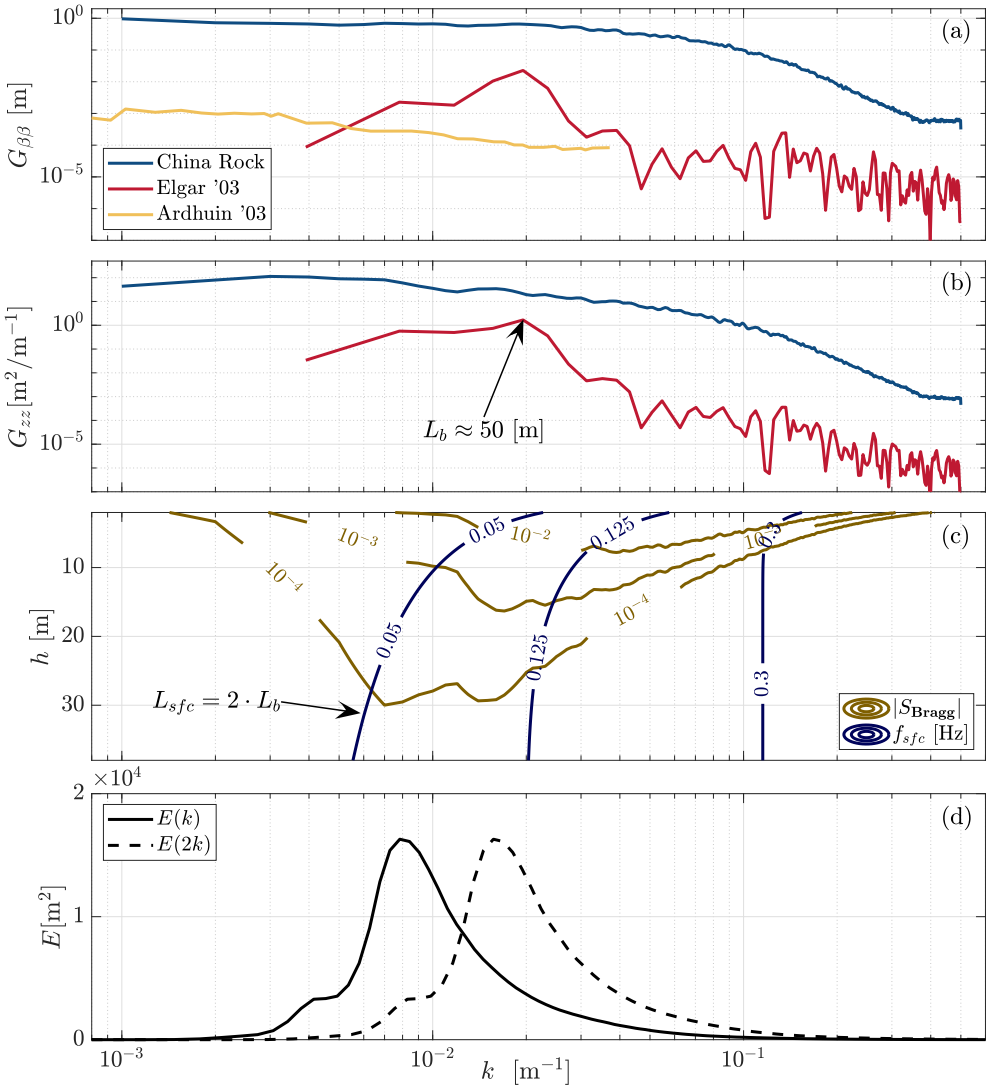

Figure 1.1. (a) Bottom slope spectrum as a function of wavenumber (k) for China Rock (blue line) as well the bottom slope spectra for North Carolina (yellow line) and Cape Cod (red line) where Bragg scattering has been observed (Ardhuin et al. 2003; Elgar et al. 2003) (b) Bottom elevation spectra as a function of k for China Rock (blue line) and Cape Cod (red line). The wavenumber of the sinusoidal sandbars are highlighted for Cape Cod Elgar et al. (2003). (c) The Bragg resonant condition as a function of k. The blue contours represent the frequency of the surface wave, which satisfies the Bragg condition for a given bottom undulation k and depth. The brown contours are the magnitude of the Bragg source term from Equation 1.5. (d) The time mean surface elevation spectrum as a function of k and $2k$ observed at China Rock.

There are a variety of instruments and corresponding methods for estimating directional spectra required herein for evaluating $\overline{R^2}$ and Bragg scattering. Instrumentation includes an array of bottom-mounted pressure sensors, sometimes with co-located current meters (Benoit et al. 1997; Dickson et al. 1995; Elgar et al. 2003), bottom-mounted acoustic Doppler current profilers (ADCPs) (Herbers et al. 1991; Herbers and Lentz 2010), and global positioning system (GPS)-based surface buoys (Herbers et al. 2012; Raghukumar et al. 2019). The computational methods for estimating directional spectra include the extended maximum entropy method (EMEM) given in Hashimoto et al. (1994), the Bayesian directional method (BDM) given in Hashimoto and Konbune (1988), and many others. Field and laboratory tests were conducted to determine the best method for the particular instrument deployed (Benoit et al. 1997; Lin et al. 2022; Lancaster et al. 2021). Arrays of synchronous observations work best, owing to the increased degrees of freedom, and the BDM is the recommended method (Benoit et al. 1997). Single point measurements from either fixed instruments or surface floating buoys are best analyzed using the EMEM, though with an underestimation for describing directional spread (Lin et al. 2022). Huntley and Davidson (1998) demonstrated through numerical simulations the applicability of directional methods in a reflective environment. GPS-based surface directional wave buoys have not been explicitly evaluated for $\overline{R^2}$, owing to their quasi-Lagrangian nature. They have been shown to reliably estimate directional spectra (Herbers et al. 2012; Raghukumar et al. 2019; Lancaster et al. 2021), and it is expected that they will provide reasonable estimates of $\overline{R^2}$, adhering to the limitations in Huntley and Davidson (1998). In the absence of a spatial bottom array, a bottom-mounted ADCP can be analyzed as a spatial array owing to the beam geometry (Herbers and Lentz 2010; Benoit et al. 1997) providing the second best estimates of wave direction. Here $\overline{R^2}$ for GPS-based buoy is tested against bottom-mounted ADCP with a modified solution for instrument tilt.

$\overline{R^2}$ and Bragg Scattering are analyzed using nearshore wave directional spectra. SS wave reflection and directional statistics are characterized at a variety of rocky and sandy shores along Monterey and Santa Cruz. Comprehensive comparisons are provided for reflection and directional spreading amongst these varying shores. The field sites, experiments, instrumentation, and processing methods are outlined in chapter two. In chapter three, statistical analysis and results are presented and discussed in chapter four. The summary and conclusions are given in chapter five, where an argument is made that estimates of reflection

at rocky shores can be improved by including the shore roughness in the estimate, which reduces wave reflection. Additionally, the comparison of reflection estimates demonstrates that GPS-based wave buoys are capable of reflection estimates equivalent to those derived from ADCPs. Finally, Bragg scattering was expected along the rocky shore at China Rock, but it was not observed and the reasons why are discussed.

CHAPTER 2:
Methods

2.1 Experiment site and Instrumentation

Wave measurements were taken with surface GPS-tracking wave buoys and bottom-mounted ADCPs over three field experiment phases off the southern sandy beaches in Monterey Bay (phase 1), the rocky shores around the Monterey Peninsula (phase 2) and the rocky platforms on the western shores of Santa Cruz (phase 3). The entire experiment area, with the location of each phase, is highlighted in Figure 2.1a, along with the beaches used to name each array (white squares). Phase 1 took place during June-July 2021 with sparse cross-shore arrays of wave buoys deployed at Sand City (SC), North Sand City (NSC), and Marina (MAR). An ADCP was colocated with a wave buoy in the middle of the Sand City array. Phase 2 was conducted during August-September 2021 with cross-shore arrays of wave buoys deployed at China Rock (CR), Asilomar (AS), and Pescadero Point (PP), and a single wave buoy was deployed at South Cypress Point. Two of the wave buoys at China Rock were colocated with an ADCPs (Figure 2.1c). The phase 3 deployment took place in August 2022, with cross-shore arrays of wave buoys at Wilder Ranch (WR), and a single wave buoy was deployed at Mitchell's Cove (MC) (Figure 2.1b). Site descriptions are provided in more detail below. The instruments varied in depth from 10 to 40 m and offshore distances from 140 m to 2 km. Distances and depths for each instrument are provided in Table 2.1.

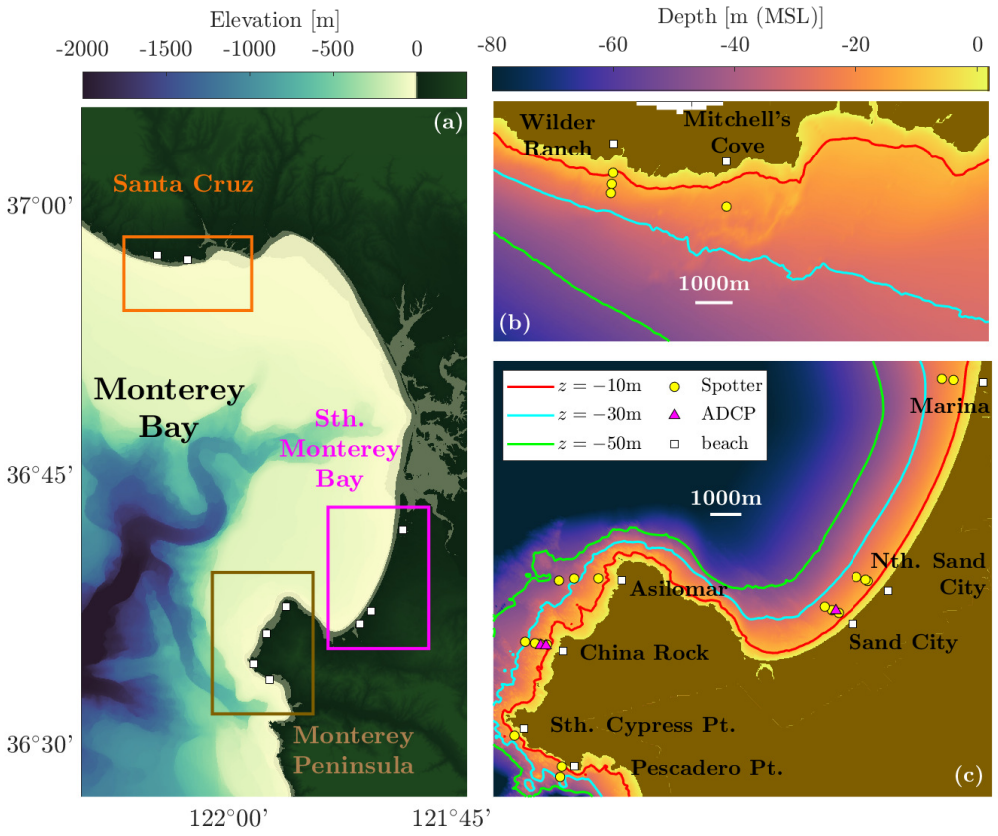

Figure 2.1. (a) Overview of the experiment sites, highlighting the location of each observation phase. Enlarged maps of the Santa Cruz site (b) and the two Monterey sites (c), wave buoys are shown as yellow circles with the ADCPs as magenta triangles. The red, cyan, and green lines highlight the 10, 30, and 50-meter isobaths. The beach used to name each array is shown by a white square. Bathymetry source: OCM Partners (2023).

The bottom-mounted, upward-facing ADCP is a Nortek Signature 1000 (1MHz) ADCP (SIG1000), and the surface GPS wave buoy is a Sofar Ocean Technology Spotter (Spotter). The SIG1000 was mounted on a small bottom-weight at China Rock and a gimballed tripod at Sand City. The SIG1000 has five beams, with four beams slanted at 25 degrees and the fifth beam is vertical. The SIG1000 has an integrated attitude and heading reference system (AHRS) and pressure sensor. SIG1000 sampled beam velocities at 2 Hz. Spotters

Table 2.1. Summary table of the experiment sites showing the deployment depth, offshore distance, beach slope β, and beach roughness, σ_{zb}. Sites are color-coded by the beach type: yellow denotes sandy beaches, orange denotes rough rocky shores, purple denotes rocky shores with cliffs, and grey denotes rocky platforms. * for instrument depth represents co-located Spotter and SIG1000

site	**depth** [m]	**distance offshore** [m]	**beach slope** β			**beach shoreline roughness** σ_{zb}		
	tide [low, middle, high]		L	M	H	L	M	H
Sand City SIG1000	10, 15*, 20 15*	490, 720, 970 620	0.09	0.14	0.14	0.02	0.03	0.04
North Sand City	10, 15, 20	470, 560, 870	0.09	0.14	0.14	0.03	0.04	0.04
Marina	12, 18	750, 1130	0.09	0.10	0.11	0.03	0.03	0.03
China Rock SIG1000	10*, 16*, 20, 30 10*, 15*	310, 540, 700, 1000 330, 500	0.09	0.15	0.18	0.08	0.12	0.13
Asilomar	15, 30, 40	635, 1300, 1730	0.09	0.09	0.10	0.08	0.09	0.10
Pescadero Point	15, 20	140, 420	0.16	0.19	0.25	0.11	0.16	0.17
South Cypress Point	15	240	0.15	0.19	0.25	0.11	0.19	0.20
Wilder Ranch	10, 17, 20	410, 700, 940	0.11	0.19	0.26	0.02	0.12	0.13
Mitchell's Cove	20	870	0.14	0.32	0.46	0.05	0.23	0.25

measure the GPS displacements at 2.5 Hz with an accuracy ± 2 cm depending on the field of view, weather conditions, and satellite availability (Sofar Ocean 2023). Hourly spectral estimates are based on a Hanning window of 200 seconds with a 50% overlap. The analysis focuses on the SS frequency band (0.05 - 0.2 Hz), where differences in Nyquist frequencies

and low-frequency GPS drifts are not an issue.

Elevation data are sourced from the United States Geological Survey coastal national elevation database (CoNED) application project, which has generated an integrated topobathymetric digital elevation model (TBDEM) covering the experiment site at 1-meter resolution (Danielson et al. 2016; OCM Partners 2023). The TBDEM is based on 70 different bathymetric and topographic surveys seamlessly combined for nearshore applications (Danielson et al. 2016; OCM Partners 2023). Beach shoreline slopes, β, are calculated from cross-shore profiles at ±5 m over the vertical relative to the mean water level. β are computed over multiple cross-shore profiles in a defined alongshore shoreline region and alongshore-averaged. The alongshore region is defined by refracting the wave directions from the buoy measurements to the shoreline by Snell's Law (Herbers et al. 1999), representing the reach that incoming waves interact with the shoreline. Beach shoreline roughness, σ_{zb}, is the standard deviation from the mean cross-shore profile for the same region.

In addition to the elevation data, visual inspections by land and sea were conducted at the experiment sites to classify the shorelines as sandy, rough rocky, rocky cliffs, or rocky platforms. β and σ_{zb} for the field sites are provided in Table 2.1, grouped by beach type with instrument depth and distance from shore. Sand City, North Sand City, and Marina are sandy with β 0.09 at low tide and increasing at high tide to 0.11 to 0.14. σ_{zb} at sandy beaches is small with little tidal variability, 0.02 to 0.04 m (Figure 2.2 ab). China Rock and Asilomar are rough rocky shorelines with quasi-periodic small rocky headlands with alternating embayments. Most embayments terminate with cobbled beaches and the occasional sandy spots, particularly at Asilomar. The headlands are rough and rocky. The rocky shore β varies from around 0.09 at low tide to 0.10-0.18 at high tide; σ_{zb} is 0.08m at low tide and 0.10-0.13 m at high tide (Figure 2.2 cd). β and σ_{zb} were smaller at Asilomar possibly owing to the inclusion of more sandy embayments. Rocky shores terminating at cliffs were observed at Pescadero Point and South Cypress Point, where β at low tide was the largest at 0.15, increasing to 0.25 at high tide, σ_{zb} varied from 0.11 to 0.20 m throughout the tidal range (Figure 2.2 ef). Wilder Ranch and Mitchell's Cove are both described as rocky platforms, with β ranging from 0.11-0.14 at low tide up to 0.26-0.46 at high tide; σ_{zb} has the largest range with the tide at rocky platforms with low tide σ_{zb} of 0.02-0.05 m are comparable to sandy beaches, and high tide σ_{zb} of 0.13-0.25 m among the roughest observed (Figure 2.2 gh). The differences between shoreline classes are also evident when

inspecting the distribution of beach profiles along the reach of incoming waves. The sandy beaches show very little variability, while the rocky shores and platforms have much greater slopes and much larger variability (Figure 2.2).

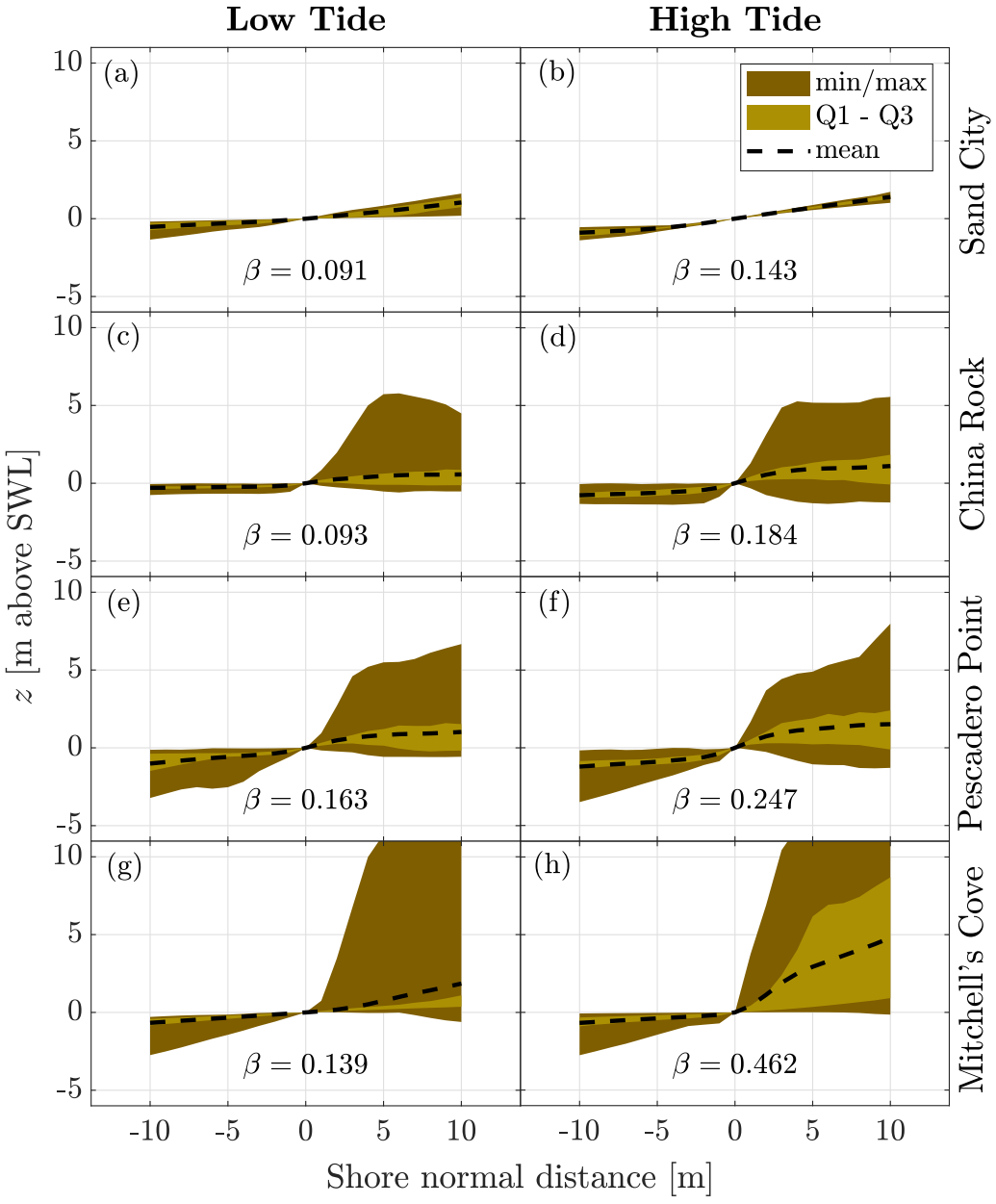

Figure 2.2. Cross-shore profiles of the alongshore average with 25% and 75% quartile and extrema variability as a function of normalized distance at low and high tide for Sand City (a) and (b), China Rock (c) and (d), Pescadero Point (e) and (f), and Mitchell's Cove (g) and (h). The mean profile is shown by the black dashed line, with the inter-quartile range shown in light brown and extrema shown in dark brown. Bathymetry source: OCM Partners (2023).

Spatially-averaged elevation and bottom slope spectra were estimated at China Rock using 350 cross-shore profiles with 1 m alongshore spacing (Figure 1.1a-b). A Hanning window was applied to each profile to limit spectral leakage. The bathymetry underwent a filtering process by applying a circular mask filter with a diameter of 100 m. This generated a low-pass bathymetry used later for estimates of shoaling and refraction (Ardhuin et al. 2003). The 1/100 m smoothing was deemed most appropriate due to large elevation gradients and the presence of cliffs at the shoreline. For these experiments, 1/100 m was applied universally.

During phase 1, the significant wave height, H_s ranged from 0.5 - 1.7 m, with the mean direction, $\overline{\theta}$, predominantly from the northwest with a very narrow distribution owing to the aperture of Monterey Bay, and the mean period, $\overline{T}$, was mostly between 6 - 10 seconds (Figure 2.3abc). H_s was larger in phase 2, ranging from 0.7 - 2.7 m, with a broader $\overline{\theta}$ distribution still predominantly from the northwest (Figure 2.3de). The distribution of $\overline{T}$ was similar to those observed during phase 1 with the addition of the occasional long swell (12-18 seconds) from the southwest (Figure 2.3f). The conditions during phase 3 were more benign with H_s mostly in the 0.5 - 1 m range, southwesterly θ_p, and $\overline{T}$ was generally between 8 - 12 seconds, which is slightly longer (on average) than the other two phases (Figure 2.3ghi).

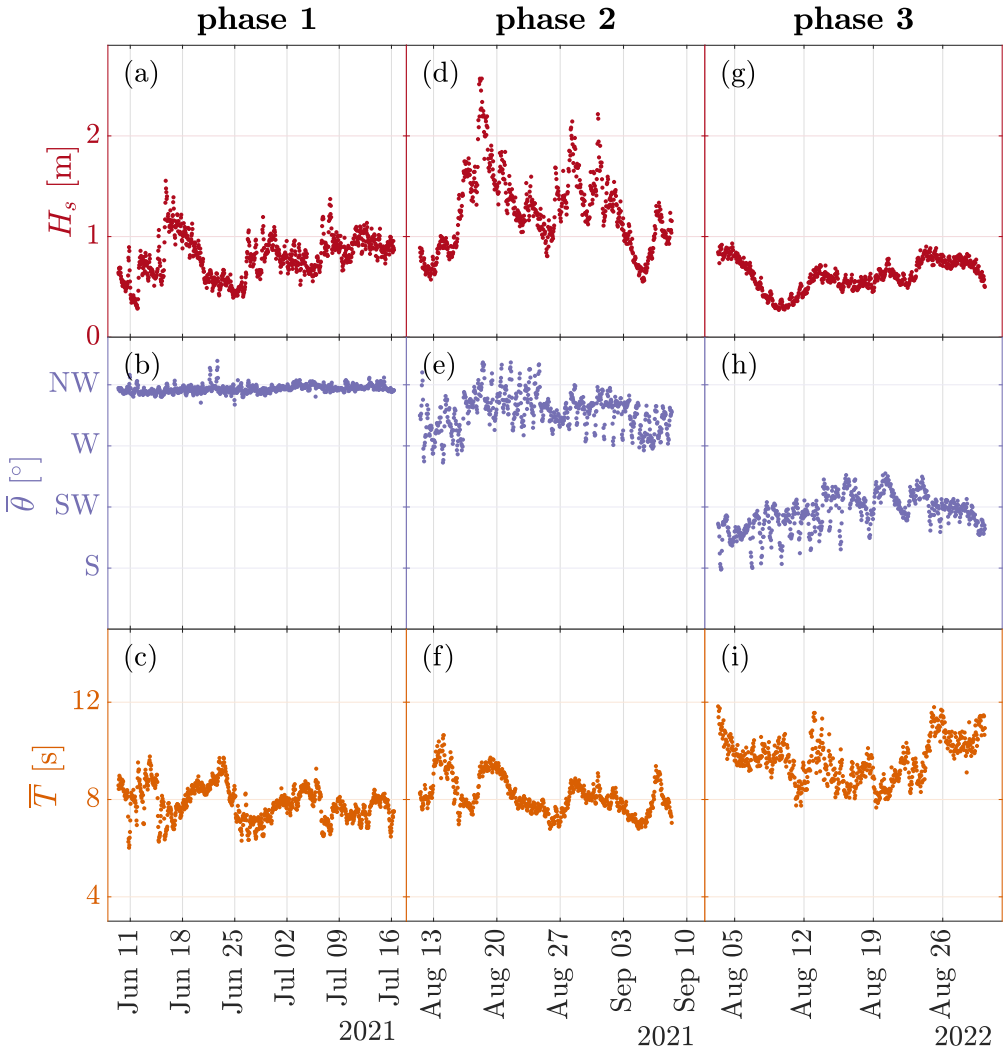

Figure 2.3. time-series of one-hour averaged significant wave height, H_s, mean wave direction, $\overline{\theta}$, and mean wave period, $\overline{T}$, for the three observational phases. Observations were obtained from Spotters at (a,b,c) Sand City at 15 m water depth, (d,e,f) China Rock at 30 m water depth, and (g,h,i) Wilder Ranch at 17 m water depth (see Figure 2.1 for mooring locations).

2.2 Directional spectra and their bulk statistics

An energy density directional spectrum $S(f,\theta)$, commonly referred to as a "directional spectrum", describes the wave variance in 2D as a function of frequency, f, and direction,

θ, (Benoit et al. 1997). A directional spectrum can be decomposed into the product of an energy density spectrum of the surface elevation, $E(f)$, and a normalized directional distribution, $D(f,\theta)$,

$$S(f,\theta) = E(f) \cdot D(f,\theta), \tag{2.1}$$

where

$$\int_0^{2\pi} S(f,\theta)\, d\theta = E(f), \tag{2.2}$$

and

$$D(f,\theta) \geq 0 \quad \text{for all } (f,\theta) \tag{2.3}$$

$$\int_0^{2\pi} D(f,\theta)\, d\theta = 1 \quad \text{for all } f. \tag{2.4}$$

$D(f,\theta)$ is characterized by the mean direction, θ_0, and directional spread, σ_θ, as a function of frequency (Kuik et al. 1988). θ_0 is the vector mean of the $D(f,\theta)$, while σ_θ is analogous with standard deviation. θ_0 is given by:

$$\theta_0(f) = \arctan\left(\frac{\int_0^{2\pi} \sin\theta\, D(f,\theta)\, d\theta}{\int_0^{2\pi} \cos\theta\, D(f,\theta)\, d\theta}\right) \tag{2.5}$$

σ_θ is then given by:

$$\sigma_\theta(f) = \sqrt{4\int_0^{2\pi} \sin^2\left(\frac{\theta - \theta_0(f)}{2}\right) D(f,\theta)\, d\theta}. \tag{2.6}$$

The energy weighted mean direction, $\overline{\theta}$ and energy weighted directional spread, $\overline{\sigma_\theta}$, are the bulk statistics of $\theta_0(f)$ and $\sigma_\theta(f)$. They are calculated by taking the energy-weighted mean of each parameter. Since the mean direction is a circular measure, a vector mean must be taken. $\overline{\theta}$ and $\overline{\sigma_\theta}$ are given by:

$$\overline{\theta} = \arctan\left(\frac{\int^{SS} w(f)\sin\theta_0(f)\,df}{\int^{SS} w(f)\cos\theta_0(f)\,df}\right) \tag{2.7}$$

and

$$\overline{\sigma_\theta} = \frac{\int^{SS} \sigma_\theta(f)\cdot E(f)\,df}{\int^{SS} E(f)\,df}, \tag{2.8}$$

where the energy weight, $w(f)$, is

$$w(f) = \frac{E(f)}{\int^{SS} E(f)\,df}. \tag{2.9}$$

It is commonplace to calculate $\theta_0, \sigma_\theta, \overline{\theta}$, and $\overline{\sigma_\theta}$ using Fourier moments (i.e., a_0, a_1, a_2, b_1, b_2) calculated directly from cross-spectral estimates for co-located observations scaled using linear wave theory (Longuet-Higgins et al. 1961; Kuik et al. 1988; Herbers et al. 2012). Longuet-Higgins et al. (1961) explicitly states that θ_0, σ_θ, $\overline{\theta}$, and $\overline{\sigma_\theta}$ can be calculated without estimating $S(f,\theta)$. However, it is only reasonable to calculate θ_0, σ_θ, $\overline{\theta}$, and $\overline{\sigma_\theta}$ using the Fourier moments for unimodal spectra.

When waves from multiple wave sources are present, it is proper to partition $S(f,\theta)$ into source components, defined by f and θ bands, such that $S(f,\theta)$ is the sum of the partitioned components,

$$S(f,\theta) = S_1(f,\theta) + S_2(f,\theta) + \ldots + S_n(f,\theta). \tag{2.10}$$

Each $S_n(f,\theta)$ is decomposed using Equation 2.1 to generate $D_n(f,\theta)$ which are subject to the conditions in Equations 2.3 and 2.4. Bulk statistics are then estimated for each spectral component from their directional distribution (Gerling 1992). A number of methods for partitioning directional spectra were developed based on spectral geometry or by defining critical energy density levels (Gerling 1992; Guillaume 1990; Hasselmann et al. 1996). The present situation is simpler, as $S(f,\theta)$ are partitioned into two directional quadrants (e.g.,

onshore and offshore) based on the shore normal direction:

$$S(f,\theta) = S_{on}(f, -90 \leq \theta \leq 90) + S_{off}(f, 90 \leq \theta \leq 270) \tag{2.11}$$

$S_{on}(f,\theta)$ and $S_{off}(f,\theta)$ are partitioned from $S(f,\theta)$ by masking the appropriate sectors in the directional spectrum. After masking, more physically meaningful bulk estimates of θ_0 and σ_θ are obtained for the partitioned sectors. This is especially the case for σ_θ, which is sensitive to directional distribution at large angles from the mean direction (Lin et al. 2022). For example, θ_0 and σ_θ for $S(f,\theta)$ are $9.1°, 37.8°$, whereas partitioned $S_{on}(f,\theta)$ and $S_{off}(f,\theta)$ results in $\theta_0, \sigma_\theta = 9.5°, 16.4°$ for onshore and $\theta_0, \sigma_\theta = 192.8°, 13.8°$ for offshore (Figure 2.4). Notice how σ_θ before partitioning is greater than the sum of the two components σ_θ calculated after partitioning.

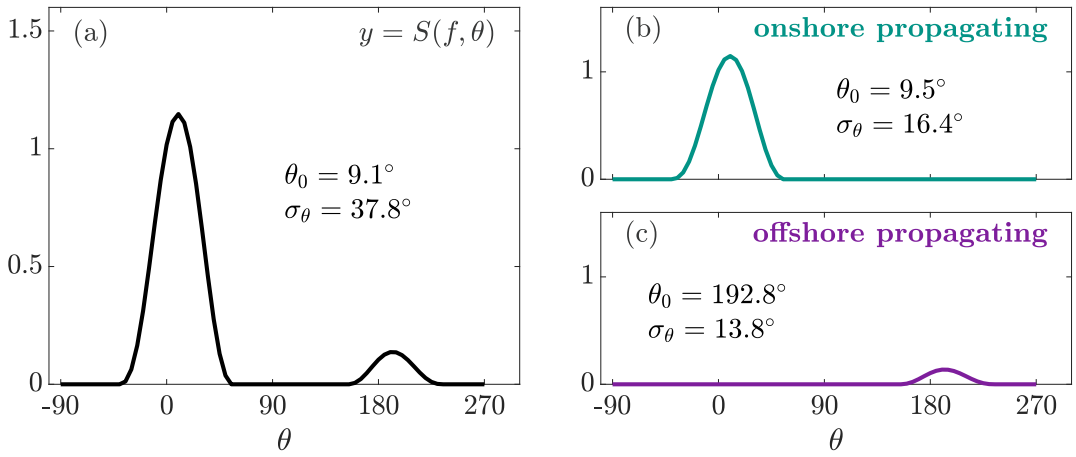

Figure 2.4. (a) The total directional spectrum for a given frequency that includes onshore propagating and offshore propagating wave components, where $\theta_0, \sigma_\theta = 9.1°, 37.8°$. (b) The onshore component is partitioned resulting in $\theta_0, \sigma_\theta = 9.5°, 16.4°$ and the offshore (c) represents $\theta_0, \sigma_\theta = 192.8°, 13.8°$

2.3 Directional spectra estimation

Directional spectra are calculated from the displacement data of the Spotter using the EMEM (Hashimoto and Konbune 1988) with an angular separation of five degrees used

to balance computational time and resolution. The displacement data are processed with the wave analysis for fatigue and oceanography (WAFO) toolbox (Brodtkorb et al. 2000). The WAFO toolbox does not support an ADCP beam velocity array (Herbers and Lentz 2010). Matsuba et al. (2022) published a BDM adapted to process ADCP beam velocity array. Both Herbers and Lentz (2010) and Matsuba et al. (2022) are designed for an ADCP deployed upright without any appreciable tilt. In order to apply the BDM to the ADCP beam velocities herein, the routines are modified to account for tilt measured by the SIG1000. The tilted method involves re-deriving the transfer function for beam velocities and applying a coordinate transformation from the instrument frame to the local tangent reference frame. The derivation of the transfer function and coordinate transformation are presented next.

The surface elevation, $\eta(\vec{\boldsymbol{x}}, t)$, of a homogeneous wave field is given by the sum of plane waves with different frequencies, f, and propagation directions, θ,

$$\eta(\vec{\boldsymbol{x}}, t) = \sum_{f} \sum_{\theta} \frac{H_{f,\theta}}{2} e^{i(\vec{\boldsymbol{k}}\cdot\vec{\boldsymbol{x}} - 2\pi f t + \varphi_{f,\theta})} \tag{2.12}$$

where $H_{f,\theta}$ is the wave height of each component per frequency and direction, $\vec{\boldsymbol{k}}$ is the wavenumber vector given by $\vec{\boldsymbol{k}} = (k\cos\theta, k\sin\theta)$, with $k := |\vec{\boldsymbol{k}}|$, $\vec{\boldsymbol{x}} = (x, y, z)$ is the position vector, and $\varphi_{f,\theta}$ accounts for the random phase of each component wave. The wavenumber vector obeys the dispersion relation in Equation 1.6.

Under linear wave theory, particle velocity $\vec{\boldsymbol{u}}(\vec{\boldsymbol{x}}, t)$ can expressed as:

$$\begin{aligned}
\vec{\boldsymbol{u}}(\vec{\boldsymbol{x}}, t) &= [u, v, w] \\
&= \left[2\pi f \frac{\cosh(k(h+z))}{\sinh(kh)} \cos\theta\, \eta, 2\pi f \frac{\cosh(k(h+z))}{\sinh(kh)} \sin\theta\, \eta, -i\, 2\pi f \frac{\sinh(k(h+z))}{\sinh(kh)}\, \eta\right] \\
&= \frac{2\pi f \cosh(k(h+z))\eta}{\sinh(kh)} [\cos\theta, \sin\theta, -i\tanh(k(h+z))]
\end{aligned}$$

where z is the vertical component of the position vector. For an arbitrary direction, defined by a unit vector $\hat{\boldsymbol{n}} := [n_x, n_y, n_z]$, the particle velocity component, $\vec{\boldsymbol{U}}_{\hat{\boldsymbol{n}}}$, can then be extracted

by projecting the velocity onto that unit vector direction by taking the dot product.

$$\begin{aligned}\vec{\boldsymbol{U}}_{\hat{\boldsymbol{n}}}(\vec{\boldsymbol{x}},t) &= \vec{\boldsymbol{u}}(\vec{\boldsymbol{x}},t)\cdot\hat{\boldsymbol{n}} \\ &= \frac{2\pi f\cosh(k(h+z))\eta}{\sinh(kh)}\left[n_x\cos\theta + n_y\sin\theta - in_z\tanh(k(h+z))\right]\end{aligned}$$

This can be rearranged to express the velocity component as the product of the surface elevation and a transfer function, $G(f,\theta)$, such that:

$$\vec{\boldsymbol{U}}_{\hat{\boldsymbol{n}}}(\vec{\boldsymbol{x}},t) = G(f,\theta)\cdot\eta(\vec{\boldsymbol{x}},t) \tag{2.13}$$

where:

$$G(f,\theta) = \frac{2\pi f\cosh(k(h+z))}{\sinh(kh)}\left[n_x\cos\theta + n_y\sin\theta - in_z\tanh(k(h+z))\right] \tag{2.14}$$

This transfer function is similar to that presented by Herbers and Lentz (2010) in their Equation 5, but here the direction is defined by a unit vector rather than azimuth and elevation. In their expression, the transfer function includes the spatial varying component ($e^{i\vec{k}\cdot\vec{x}}$), and the leading term is expressed differently by using the dispersion relation. They express direction by rotation angles about the x and z axes rather than by unit vector components. While this is mathematically equivalent, we apply multiple angular transformations first to account for the beam geometry and then to account for instrument tilt. By defining direction by a unit normal, it was a simpler and more intuitive transformation.

Unit vectors in each of the beam directions must be transformed from the instrument relative frame into the local tangent plane. The beam slant angle, α, of the SIG1000 is 25 degrees. The unit vector of beams one through four are given by:

$$\hat{\boldsymbol{n}}_{I1} = \begin{bmatrix}\sin\alpha\\0\\\cos\alpha\end{bmatrix} \qquad \hat{\boldsymbol{n}}_{I2} = \begin{bmatrix}0\\-\sin\alpha\\\cos\alpha\end{bmatrix} \qquad \hat{\boldsymbol{n}}_{I3} = \begin{bmatrix}-\sin\alpha\\0\\\cos\alpha\end{bmatrix} \qquad \hat{\boldsymbol{n}}_{I4} = \begin{bmatrix}0\\\sin\alpha\\\cos\alpha\end{bmatrix} \tag{2.15}$$

The subscript denotes the beam number, and the subscript I denotes the instrument reference frame. The transformation must account for magnetic deviation, and instrument heading, pitch, and roll $(\theta_d,\theta_h,\theta_p,\theta_r)$. The sense of all of these angles is prescribed in the

instrument documentation (Nortek 2017). For completeness, the transformation is broken into components to show the transformation for each angle.

$$\mathbf{T}_{head\ and\ dev} = \begin{bmatrix} \sin(\theta_h + \theta_d) & -\cos(\theta_h + \theta_d) & 0 \\ \cos(\theta_h + \theta_d) & \sin(\theta_h + \theta_d) & 0 \\ 0 & 0 & 1 \end{bmatrix} \tag{2.16}$$

$$\mathbf{T}_{pitch} = \begin{bmatrix} \cos\theta_p & 0 & -\sin\theta_p \\ 0 & 1 & 0 \\ \sin\theta_p & 0 & \cos\theta_p \end{bmatrix} \tag{2.17}$$

$$\mathbf{T}_{roll} = \begin{bmatrix} 1 & 0 & 0 \\ 0 & \cos\theta_r & -\sin\theta_r \\ 0 & \sin\theta_r & \cos\theta_r \end{bmatrix} \tag{2.18}$$

then the total transformation is given by:

$$\mathbf{T} = \mathbf{T}_{head\ and\ dev}\ \mathbf{T}_{pitch}\ \mathbf{T}_{roll} \tag{2.19}$$

Finally, each unit vector is translated:

$$\hat{\boldsymbol{n}}_k = \mathbf{T}\hat{\boldsymbol{n}}_{Ik} \qquad \text{for} \qquad k = 1, 2, 3, 4 \tag{2.20}$$

so that data from each beam of the SIG1000 can be properly transformed into the local tangent frame. This is then the unit vector $\hat{\boldsymbol{n}} = [n_x, n_y, n_z]$ required for to define the transfer function in Equation 2.14.

2.4 Additional considerations near a reflector

Methods to estimate directional spectra that assume the wave field is spatially homogeneous are categorized as "non-phase locked". Phase-locked methods account for the pattern of nodes and antinodes near a reflector (Huntley and Davidson 1998). The EMEM and BDM are non-phased locked methods, so care must be taken to ensure that they are only applied to observations far enough from a reflector. The applicability of the non-phase locked

method is defined by the ratio of the wave travel time, TT, to the spectral window length, WL (Huntley and Davidson 1998). TT is the time that the wave travels from the sensor to the reflector and back. Theoretically, non-phase locked methods are only applicable when $TT/WL > 1$ representing no angular degradation. Simulations found that a non-phase locked method shows little angular degradation for $0.5 < TT/WL < 1$ and only exhibited slight angular degradation for $0.2 < TT/WL < 0.5$, where the angular resolution should be doubled (Huntley and Davidson 1998). The TT defines the maximum WL, which defines the frequency resolution. For $WL = 200$ s, TT/WL was calculated for every sensor using the lowest frequency in the SS band, representing the fastest propagating wave, over the smoothed bathymetry. All sites have a $TT/WL > 0.5$ except for the Spotter at South Cypress Point and the shallowest Spotter at Pescadero Point, which had $TT/WL > 0.2$ suggesting slight angular degradation. Based on these computations and considering the 180° sectors for onshore and offshore, the directional spectra are believed to be reasonably described by the proposed non-phase lock methods.

THIS PAGE INTENTIONALLY LEFT BLANK

CHAPTER 3:
Results

3.1 Sea-Swell Reflection

$\overline{R^2}$ for SS waves averaged over one-hour were observed with a Spotter and a co-located SIG1000 at Sand City and China Rock. At Sand City, there is significant temporal variability in $\overline{R^2}$ that ranges from 0 to 0.22, with both the Spotter and SIG1000 giving similar estimates (Figure 3.1a). $\overline{R^2}$ is inversely modulated by synoptic variability in H_s with temporal maxima occurring at high tides showing the dependence on β (Figure 3.1abc). There is markedly less temporal variability in $\overline{R^2}$ at China Rock, which ranges from 0 to 0.08 (Figure 3.1d). There is some indication that $\overline{R^2}$ is also inversely modulated by H_s, with the largest $\overline{R^2}$ recorded at the minimum H_s (figure 3.1de). The clear tidal trend observed at Sand City $\overline{R^2}$ is minimal at China Rock. The Spotter appears to capture elements of tidal signal in addition to the synoptic H_s signal, whereas the SIG1000 only captures the synoptic H_s signal. Though the deployment dates differ, $\overline{T}$ similarly varied between 6 - 9 seconds for both sites (Figure 2.3c,f).

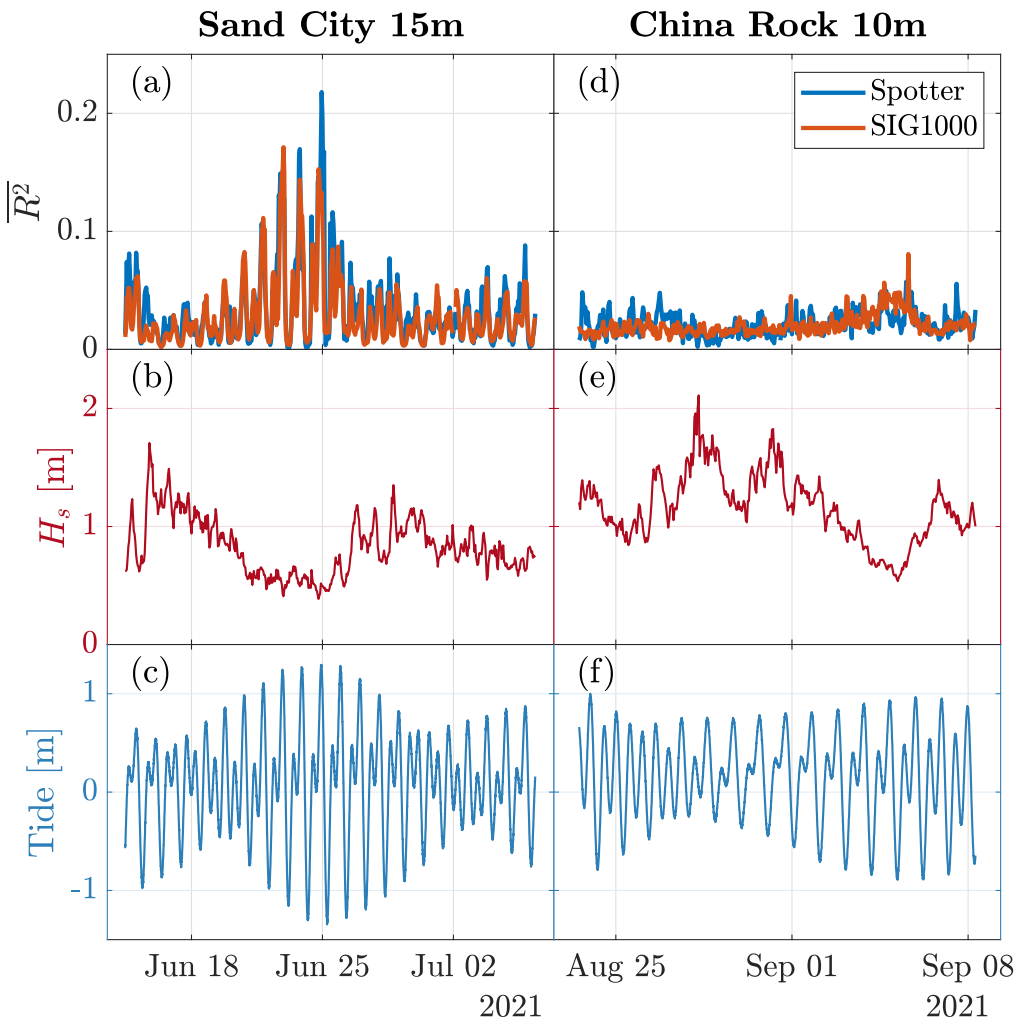

Figure 3.1. (a) Time series of $\overline{R^2}$ at Sand City in 15m depth where a Spotter and SIG1000 were co-located and co-deployed. (b) H_s measured by the Spotter during the period of co-deployment. (c) The tide record during the period of co-deployment. (d)-(f) are as (a)-(c), but for China Rock in 10m depth.

The performance of the quasi-Lagrangian Spotter to measure $\overline{R^2}$ has not been previously reported and is compared to $\overline{R^2}$ estimates derived from the spatial array of Eulerian beam velocities from the SIG1000. For Sand City, a linear regression analysis was conducted between the $\overline{R^2}$ estimates from the Spotter and SIG1000, with the intercept set to 0. The

Spotter and SIG1000 $\overline{R^2}$ estimates correlated with a r^2 coefficient of 0.70. The Spotter had a positive bias of 0.006. The gradient of the line of best fit was 1.09 with a 95% confidence interval of 1.04 - 1.14 (Figure 3.2). A χ^2 goodness of fit test was conducted between the 620 hourly $\overline{R^2}$ estimates from each instrument and the two estimates fit with a significance level of 0.05. Given the low magnitude of $\overline{R^2}$ at China Rock, the linear regression and goodness of fit test were not informative. The $\overline{R^2}$ estimates for both instruments during co-deployment was 0.02 with a standard deviation of 0.01. The $\overline{R^2}$ estimates from both instruments at China Rock exhibit similar temporal variability in terms of magnitude and trend (Figure 3.1d).

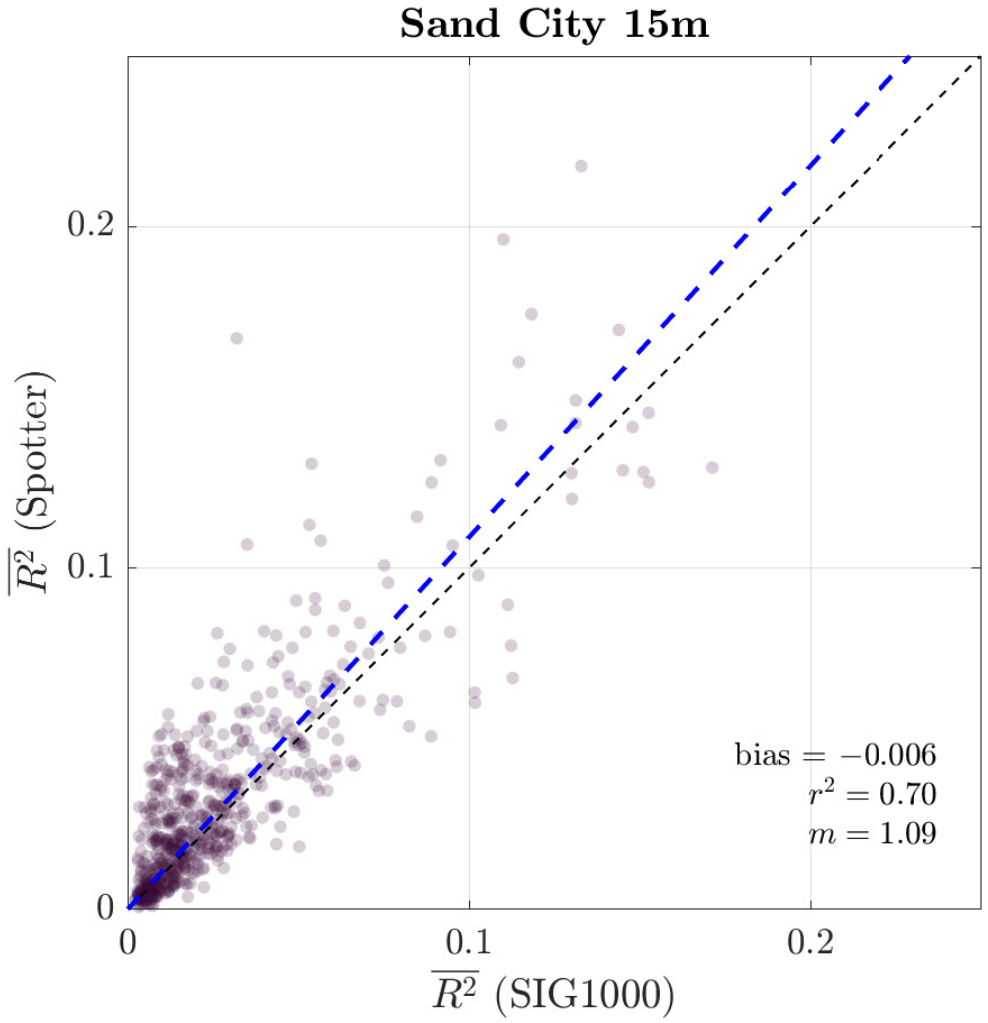

Figure 3.2. $\overline{R^2}$ estimates from the SIG1000 plotted as a function of $\overline{R^2}$ estimates from the Spotter. A linear regression was conducted between the estimates. The regression coefficient, r^2 is 0.70. The line of best fit through the origin has a gradient of 1.09 with a 95% confidence interval of 1.04 - 1.14. The Spotter had a positive bias of 0.006.

The hourly energy weighted SS band reflection $\overline{R^2}$, with the minimum, 25%, 50% (median), 75% quartiles (Q_1, Q_2, Q_3), and maximum are described for the sandy, rough rocky, and rocky platform for phases 1-3 for Spotter observations only. In addition, the mean energy weighted reflection over the whole record, $\langle\overline{R^2}\rangle$, is provided. $\langle\overline{R^2}\rangle$ varies from 0.02 to 0.12 amongst the beach types (sandy, rocky, cliff, platform) with minimal inter-variability within

each beach type (Figure 3.3a). Starting with sandy shores, $\langle\overline{R^2}\rangle$ is around 0.03 with a Q_3 of around 0.05 for southern Monterey beaches (Sand City (SC), North Sand City (NSC), Marina (MAR)). The $\langle\overline{R^2}\rangle$ is approximately 0.02 with a Q_3 of 0.04 for the rough, rocky shores (Asilomar (AS), China Rock (CR)) at the outer edge of the Monterey Peninsula. The rough, rocky cliffs (Pescadero Point (PP), South Cypress Point (SCP)) along the southern side of the Monterey Peninsula support a $\langle\overline{R^2}\rangle$ of about 0.05 with Q_3 of 0.06. For rocky platforms, $\langle\overline{R^2}\rangle$ is largest at about 0.12 with a Q_3 of 0.15. Since $\overline{R^2}$ is a function of β, H_s, and $\overline{f}$, it can be misleading to consider $\langle\overline{R^2}\rangle$ in isolation. For example, China Rock and Sand City have similar $\langle\overline{R^2}\rangle$, yet Sand City supported large $\overline{R^2}$ that occurred with low waves and higher tides. Therefore maximum $\overline{R^2}$ are examined. The maximum $\langle\overline{R^2}\rangle$ at the sandy beaches ranges from 0.14 to 0.23 and is much larger than the maximum observed at the rough rocky shores 0.05-0.08. The rocky cliffs support a maximum $\overline{R^2}$ of 0.09 - 0.14, with the largest maximum $\overline{R^2}$ at the rocky platforms, measured at 0.16 - 0.30. $\langle\overline{R^2}\rangle$ highlights differences amongst beach types with similar estimates clustered within each beach type.

$\overline{R^2}$ is subdivided into three tidal elevations (low, mid, and high) to quantify the changes in β that vary with the tide (Figure 2.2 and Table 2.1). The sandy shores show a large dependence on the tide, where low tide $\overline{R^2}$ are typically small (< 0.02) increasing at mid-tide and are largest at high tide, $\langle\overline{R^2}\rangle$ ranging from 0.04 - 0.08 (Figure 3.3b). There is no appreciable trend in $\overline{R^2}$ with the tide at the rough rocky shores, and there is only a slight increase at the rocky cliffs despite a clear tidal dependence on β (Figure 2.2c-f). For rocky platforms, there is a clear increase in $\overline{R^2}$ with the tide (Figure 3.3b), consistent with the change in β with the tide (Figure 2.2g-h).

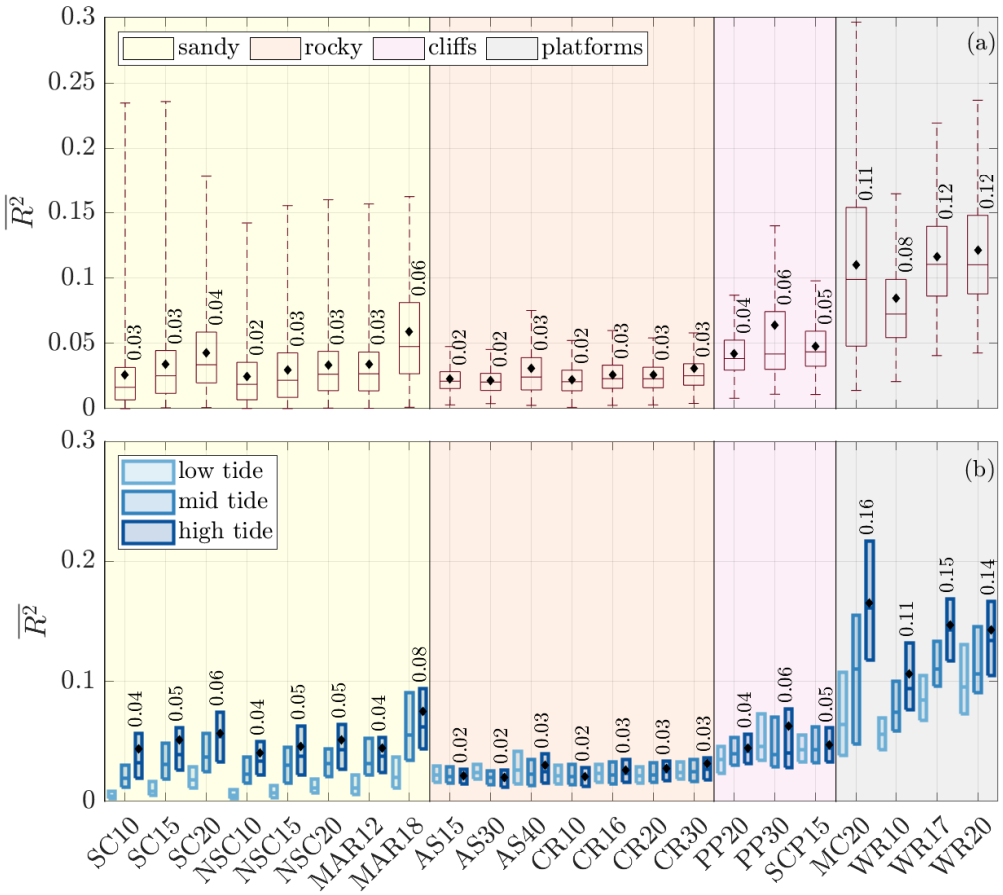

Figure 3.3. (a) boxplot of $\overline{R^2}$ at each site showing the minimum, first quartile, median, third quartile, and maximum. The time-mean $\overline{R^2}$ at each site is denoted by the black diamond, with the magnitude printed above each box. (b) as per (a), but divided by the height of the tide. Only the time-mean $\overline{R^2}$ for high tide is printed above the respective box. Sites are grouped by the shore type and color-coded, Sandy shores are yellow, rocky shores are orange, rocky shores with cliffs are purple, and rocky platforms are grey. The beaches are identified by the 2 or 3-letter beach code, Sand City (SC), North Sand City (NSC), Marina (MAR), Asilomar (AS), China Rock (CR), Pescadero Point (PP), South Cypress Point (SCP), Mitchell's Cove (MC), and Wilder Ranch (WR). The numerals following the beach code denote the average depth at the site.

3.2 Sea-Swell Directional Statistics

The variability of $\overline{\theta}$ and $\overline{\sigma_\theta}$ for incoming and outgoing SS waves as a function of beach type is discussed next. For most sites, $\overline{\theta}$ is nearly specular, consistent with observations by Elgar et al. (1994). The range of incoming angles is small (0° - 20°) at sandy and rocky shores, though larger (-8° to 45°) at rocky shores with cliffs and rocky platforms (Figure 2.3d,e,f). The larger incident angles at PP20, PP30, SCP15 are likely owing to the difficulty of defining shore normal in the absence of uniform gradients in elevation. The shoreline geometry at PP and SCP, located on the Monterey Peninsula, permits a larger range of incoming wave angles. The onshore $\overline{\sigma_\theta}$ is relatively narrow for all sites owing to wave refraction. Variations in onshore $\overline{\sigma_\theta}$ across the beach types are due to their geographic setting, wave source, where the shoreline orientation will limit waves to certain directions. For example, sandy beaches are influenced by the aperture of the Monterey Peninsula and the Santa Cruz headland. Likewise, south-facing shorelines will only be associated with waves from the south. Understanding how onshore $\overline{\sigma_\theta}$ differs from the offshore $\overline{\sigma_\theta}$ is of scientific interest with regards to reflection. The offshore $\overline{\sigma_\theta}$ is generally double that of the onshore $\overline{\sigma_\theta}$. The mechanism for this increase at sandy beaches is likely owing to the persistent rip channel morphology at Southern Monterey Bay (MacMahan et al. 2004) and rip currents due to wave-current interaction (Henderson et al. 2006; MacMahan et al. 2008). The unbroken onshore waves travel across the surf zone, reflect, and travel back across the surf zone. The waves will be refracted by the surf zone rip channel morphology and the spatially-varying current field, ultimately increasing the offshore directional variability. At rocky shores, it is the large morphological variability in bottom composition and the varied shoreline orientations that are likely responsible for the increase in $\overline{\sigma_\theta}$ (Figure 3.4b). For low (< 0.03) $\overline{R^2}$, $\overline{\theta}$ and $\overline{\sigma_\theta}$ are likely insignificant, e.g., rough rocky shores and at low tides for sandy shores.

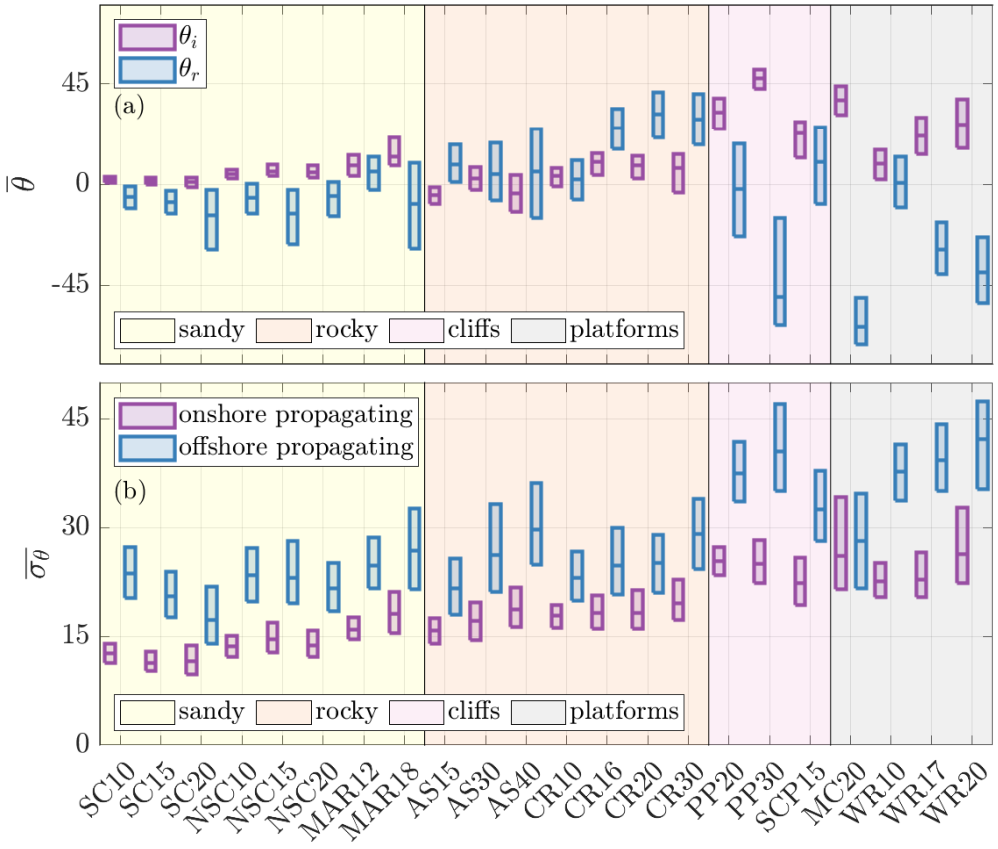

Figure 3.4. (a) Onshore and offshore propagating $\overline{\theta}$ per field site. The offshore propagating direction is converted to an angle of reflection to illustrate the specular nature of reflection. (b) Onshore and offshore propagating $\overline{\sigma_\theta}$ per field site. Sites are color-coded by beach type as described in figure 3.3

3.3 Cross-shore reflection and directional variability at China Rock

The cross-shore array at China Rock describes the spatial variability in $\overline{R^2}$ and $\overline{\sigma_\theta}$. Instrument deployment and recovery times varied slightly but were co-deployed for 540 hours between 11 August 2021 - 03 September 2021. $\langle \overline{R^2} \rangle$ is small and spatially similar from 0.027 at the deepest Spotter to 0.021 at the shallowest Spotter. $\overline{\sigma_\theta}$ narrows across the array from deep to

shallow water. The time-mean energy weighted directional spread, $\langle\overline{\sigma_\theta}\rangle$ is 21.7° at the 30m Spotter, then gradually reduced to 17.6° by the 10m Spotter. $\overline{\sigma_\theta}$ were shoaled from offshore to shallow water using the smoothed (low-passed) bathymetry to determine if $\overline{\sigma_\theta}$ narrows as predicted by Snell's Law (Herbers et al. 1999). The observed and predicted $\langle\overline{\sigma_\theta}\rangle$ were within ~3° (Figure 3.5b). The ratio of observed to predicted $\langle\overline{\sigma_\theta}\rangle$ (and the 95% confidence interval) along the array are 1.05 (1.04 - 1.07) at the 20m Spotter, 1.08 (1.06 - 1.10) at the 16m Spotter and 1.24 (1.22 - 1.26) at the 10m Spotter. This ratio of observed to predicted σ_θ is similar to sandy beaches for unbroken waves (Herbers et al. 1999).

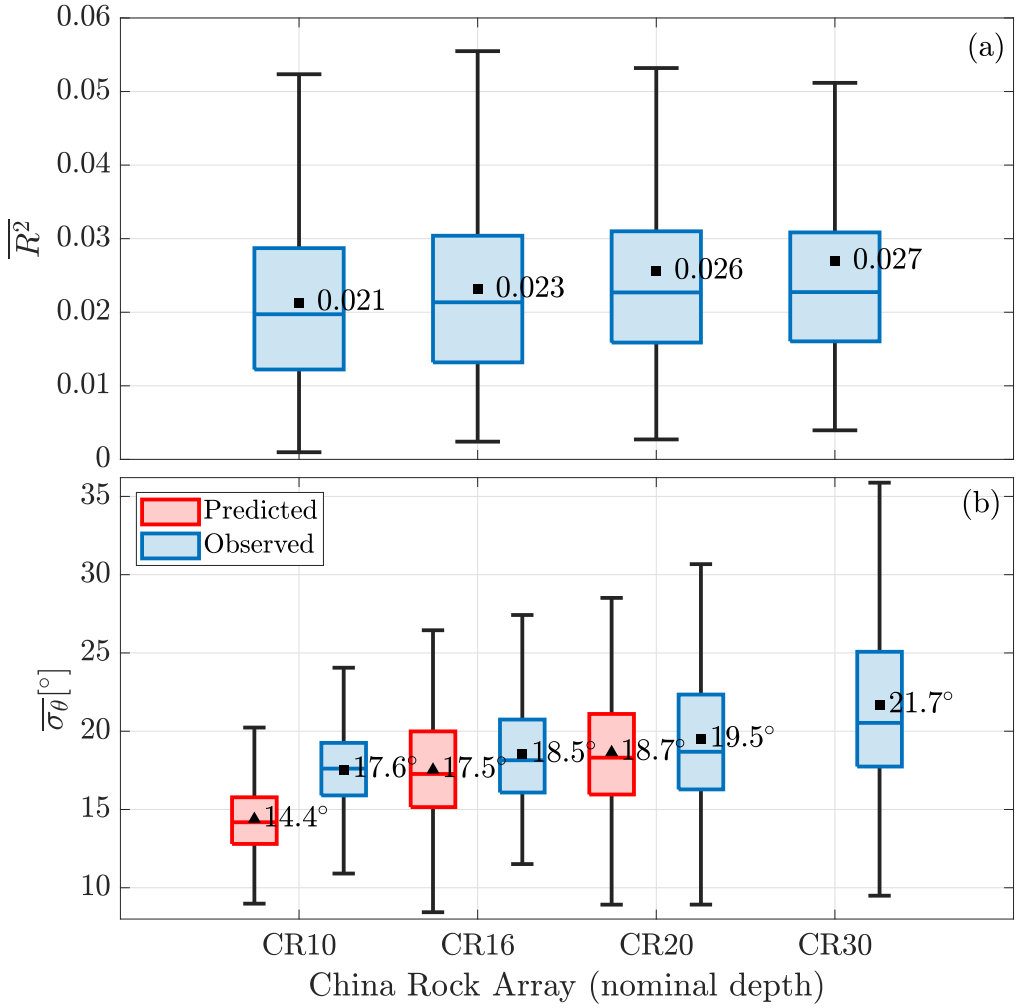

Figure 3.5. (a) A boxplot of $\overline{R^2}$ at China Rock, $\langle\overline{R^2}\rangle$ are plotted as black squares with their magnitude printed alongside. (b) A boxplot of $\overline{\sigma_\theta}$ at China Rock. The blue boxes are the observed $\overline{\sigma_\theta}$ from the Spotter buoys, and the red boxes are the predicted spread based on the immediate offshore sensor and Snell's Law (Herbers et al. 1999). Time mean measured and predicted $\overline{\sigma_\theta}$ are plotted as black squares (observations) and triangles (predictions) with the magnitude printed alongside.

CHAPTER 4:
Discussion

4.1 Rocky Shore Bragg Scattering Not Observed

If Bragg scattering were present at China Rock, it would have either caused an increase in $\overline{R^2}$ with increasing depth for backward scattering (Elgar et al. 2003) or an increase in $\overline{\sigma_\theta}$ with decreasing depth for forward scattering (Ardhuin et al. 2003). Although significant bathymetric variability could support Bragg scattering at China Rock (Figure 1.1), there was no appreciable change in $\overline{R^2}$ along the China Rock array (Figure 3.5a), nor was the change in $\overline{\sigma_\theta}$ significantly different from the directional narrowing due to shoaling (Figure 3.5b). According to Ardhuin and Herbers (2002), Bragg scattering requires interactions over more than a few wavelengths for development, which is ambiguous but may be a fundamental necessity. The max $\left(S_{Bragg}\right)$ from Equation 1.5 for the bathymetry at Cape Cod, MA is between 10^{-2} - 10^{-3} in the depth and wavenumber range of observed scattering, which is similar in magnitude to max $\left(S_{Bragg}\right)$ for China Rock in deeper depths (Figure 4.1a-b). Elgar et al. (2003) observed Bragg scattering that developed over four bottom undulations. For $k = 8 \times 10^{-3}$ m^{-1} at China Rock for backward Bragg scattering, this requires bottom undulations that are approximately 65 m long. Approximately ten bottom undulations occur across the array, which is believed to be sufficient, yet backward Bragg scattering was not observed. For forward Bragg scattering, the required bottom undulations are larger at 125-500 m, which results in two to five within the array footprint. This is likely insufficient to allow the wave-bottom interactions to develop forward Bragg scattering to a detectable level.

There are two distinct differences between the bathymetry at China Rock and Cape Cod. Firstly, the bottom slope and elevation spectra at Cape Cod have a singular peak at $k = 0.02$ m^{-1} (Figure 1.1a-b, red line), while the bottom slope and elevation spectra at China Rock have larger variance and are more indicative of random white noise. Secondly, the bottom slope at Cape Cod is very gently sloping (1:200) and can be considered uniform, whereas the slope at China Rock is steeper (1:50) and more spatially varying. These differences cause varying resonant conditions at China Rock as a function of depth, making it difficult

to achieve resonant conditions at multiple wavelengths. For Ardhuin et al. (2003), the focus was on the shelf with small profile slopes. As a result, we believe that the combination of the multi-scale nature of the bottom that occurs on a moderate sloping profile at China Rock does not allow for the development of Bragg scattering to meet the requirement of multiple wavelengths, even though there is significant amplitude in the bottom undulations at the appropriate scales.

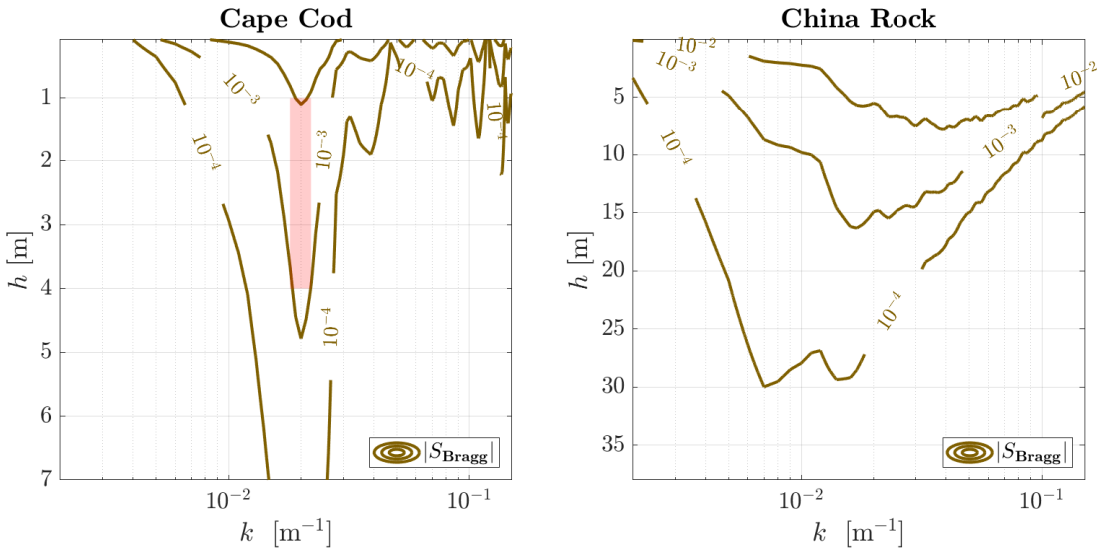

Figure 4.1. The Bragg resonant condition at (a) Cape Cod Bay, MA and (b) China Rock (similar to Figure 1.1c). The brown contours show the magnitude of the Bragg source term from Equation 1.5. The wavenumber and depth range over which Bragg scattering occurred at Cape Cod is highlighted in red.

4.2 New Wave Reflection Index for Rocky and Sandy Shores

Wave reflection indices are evaluated for rocky shores. In addition to the Miche number, M, $\overline{R^2}$ can be estimated from the Iribarren number, ξ, given by

$$\xi = \frac{\tan\beta}{\sqrt{H_\infty / L_0}}, \tag{4.1}$$

where L_0 is the deep water wavelength. Then $\overline{R^2}$ is estimated by,

$$\overline{R^2} \approx \left(0.1\xi^2\right)^2 \tag{4.2}$$

(Battjes 1974; Shanks et al. 2015). The estimates of $\overline{R^2}$ from M and ξ are nearly identical, so only M estimates are compared with the observed $\overline{R^2}$ and denoted with a subscript M. For sandy shores, most of the $\overline{R^2_M}$ values follow a 1:1 line, but there is a cluster of $\overline{R^2}$ that are smaller (Figure 4.2a). These results are similar to those of Elgar et al. (1994) for sandy shores, except for the cluster of smaller $\overline{R^2}$. For rough, rocky shores, $\overline{R^2_M}$ are constant and do not follow the 1:1 line (Figure 4.2b). The $\overline{R^2}$ values for other rocky shores are not well predicted by M or ξ. $\overline{R^2_M}$ values are clustered above the 1:1 line for rocky shores with cliffs. For rocky platforms, $\overline{R^2_M}$ values are scattered, with mostly overestimates and some underestimates (Figure 4.2d). M and ξ are not applicable for describing $\overline{R^2}$ off rocky shores.

In general, $\overline{R^2}$ is inversely proportional to wave energy and frequency and proportional to beach slope. A new reflection parameter, $\overline{R^2_P}$, is based on ξ but modified so that it includes σ_{zb},

$$\overline{R^2} \approx \overline{R^2_P} = 2.78 \times 10^{-3} \cdot \frac{\tan\beta}{H^2_\infty / L_0} \left(1 - \sigma_{zb}\right). \tag{4.3}$$

σ_{zb} represents the alongshore shoreline roughness, which is believed to reduce wave reflection. The inclusion of σ_{zb} reduces the effective beach slope. For sandy shores σ_{zb} is minimal, so the effective beach slope is the actual beach slope, however at rocky shores σ_{zb} is larger, so the effective beach slope is markedly reduced. The empirical coefficient (2.78×10^{-3}) was estimated by a linear fit on all data. $\overline{R^2_P}$ clusters fall along the 1:1 line for all beach types (Figure 4.2e-h). A linear regression analysis was conducted between each estimator and $\overline{R^2}$. When considering all beaches, r^2 is 0.07 for $\overline{R^2_M}$ and 0.45 for $\overline{R^2_P}$. For sandy beaches, r^2 is 0.32 for $\overline{R^2_M}$ and 0.36 for $\overline{R^2_P}$ and $\overline{R^2}$. Overall, including shoreline roughness as represented by σ_{zb} provides a new estimator that can predict wave reflection for various beach types, including sandy and rocky shores.

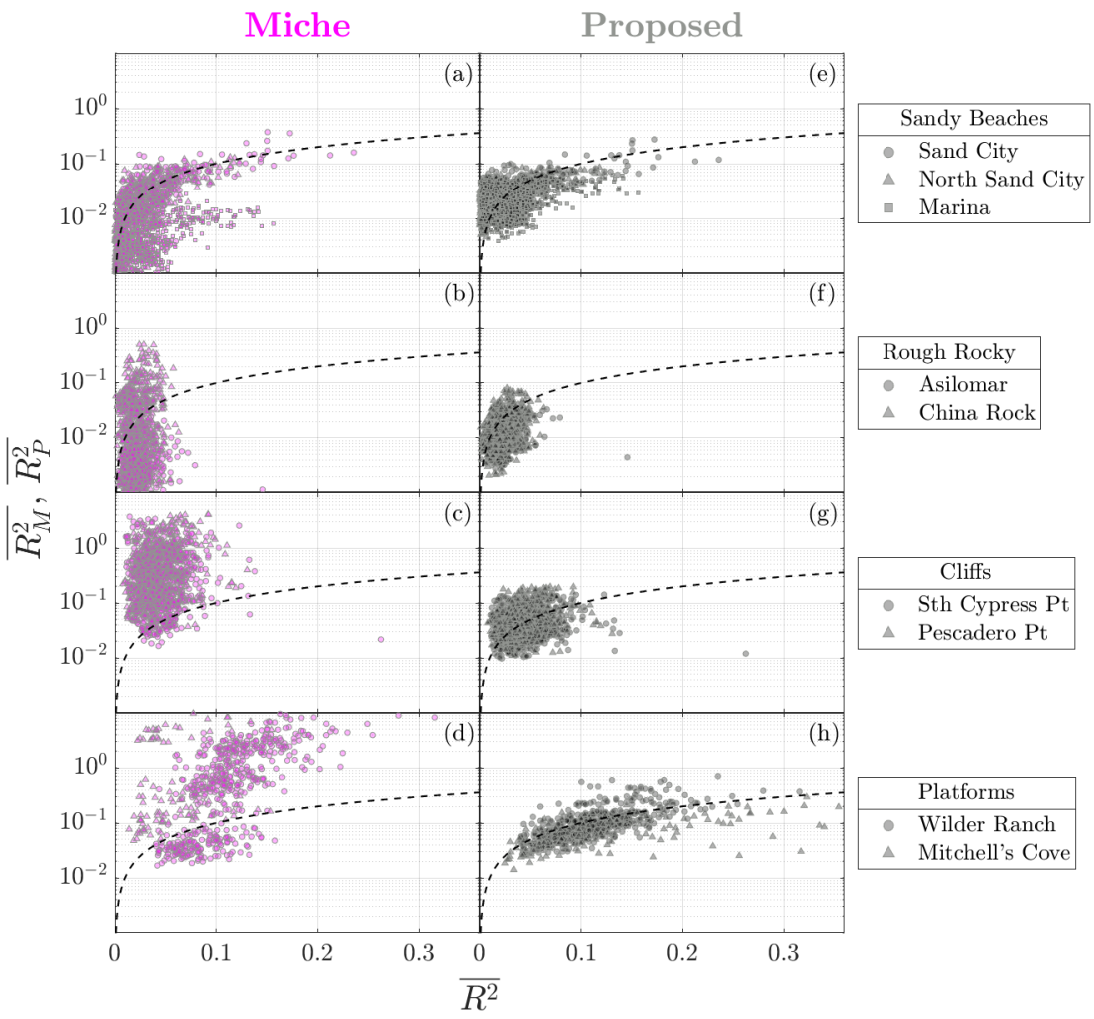

Figure 4.2. $\overline{R^2}$ estimates using the Miche number, $\overline{R_M^2}$, for (a) sandy beaches, (b) rough rocky shores, (c) rocky shores with cliffs, and (d) rocky platforms. $\overline{R^2}$ estimates using the new proposed estimator, $\overline{R_P^2}$, (e) - (h) for the same respective beaches.

CHAPTER 5:
Conclusion

The study investigated shoreline reflection and Bragg scattering of sea-swell band waves on nine shores stretching from the Monterey Peninsula to Santa Cruz, CA. The shoreline types included rough rocky, rocky cliffs, rocky platforms, and sandy beaches with varying beach slopes and shoreline roughness. GPS-based wave buoys (Spotters) and bottom-mounted acoustic Doppler current profilers (SIG1000) were deployed as cross-shore arrays at six sites and single moorings at three sites, between 10 and 40 m depth. Directional spectra were estimated using the extended maximum entropy method for the quasi-Lagrangian Spotter and the Bayesian directional method for the Eulerian SIG1000 beam velocities in a tilted frame of reference. Wave reflections are derived from the directional spectra. The correlation of wave reflection between the Spotter and SIG1000 was 0.7, with a small positive bias of approximately 0.6% for the Spotter.

The results found that wave reflection of the sea-swell energy varied by shoreline type, with sandy shores reflecting up to 23%, rough rocky shores reflecting up to 8%, rocky shores with cliffs reflecting up to 14%, and a maximum of 30% recorded at rocky platforms. Sandy shore reflection is consistent with previous empirical parameterizations, which predict reflection as a function of wave height, wave frequency, and beach slope. However, these estimators perform poorly at rocky shores, where they typically overestimate reflection, particularly when the beach slope and shoreline roughness are significant. A new estimator is proposed that accounts for the decrease in reflection with increasing beach roughness while having a similar form to previous estimators. The new estimator performed well across the range of beach slope and shoreline roughness along the varied shores. The shoreline roughness decreases reflection along rocky shores contrary to expectations of higher reflection owing to their steeper slopes.

The study expected to find Bragg scattering along the rocky shores due to the presence of large amplitude roughness occurring at the appropriate scales. However, neither increased reflection nor increased directional spread was found. The absence of Bragg scattering is believed to be associated with the non-uniformity of the bottom roughness and the moderate

bottom profile slope that leads to an insufficient number of wave-bottom interactions for development.

List of References

Ardhuin, F., and T. H. Herbers, 2002: Bragg scattering of random surface gravity waves by irregular seabed topography. *Journal of Fluid Mechanics*, **451**, 1–33, https://doi.org/10.1017/s0022112001006218.

Ardhuin, F., W. C. O'Reilly, T. H. C. Herbers, and P. F. Jessen, 2003: Swell transformation across the continental shelf. Part I: Attenuation and directional broadening. *Journal of Physical Oceanography*, **33**, 1921 – 1939, https://doi.org/10.1175/1520-0485(2003)033<1921:STATCS>2.0.CO;2.

Bascom, W. N., 1951: The relationship between sand size and beach-face slope. *Eos, Transactions American Geophysical Union*, **32**, 866–874, https://doi.org/https://doi.org/10.1029/TR032i006p00866.

Battjes, J. A., 1974: Surf similarity. *14th Coastal Engineering Conference*, Copenhagen, Denmark, 466-480, https://doi.org/10.9753/icce.v14.26.

Benoit, M., P. Frigaard, and H. A. Schäffer, 1997: Analysing multidirectional wave spectra. *27th IAHR Congress*, San Francisco, USA.

Bird, E. C. F., 2011: *Coastal geomorphology: An Introduction*. 2nd ed., John Wiley & Sons, 436 pp.

Brodtkorb, P. A., P. Johannesson, G. Lindgren, I. Rychlik, J. Rydén, and E. Sjö, 2000: WAFO - a matlab toolbox for the analysis of random waves and loads. *Proc. 10'th Int. Offshore and Polar Eng. Conf., ISOPE*, Seattle, USA, 343-350.

Danielson, J. J., S. K. Poppenga, J. C. Brock, G. A. Evans, D. J. Tyler, D. B. Gesch, C. A. Thatcher, and J. A. Barras, 2016: Topobathymetric elevation model development using a new methodology: Coastal national elevation database. *Journal of Coastal Research*, **76**, 75–89, https://doi.org/10.2112/SI76-008.

Dean, R. G., and R. A. Dalrymple, 1991: *Water Wave Mechanics for Engineers and Scientists*, Vol. 2. World Scientific, 353 pp.

Dickson, W. S., T. H. C. Herbers, and E. B. Thornton, 1995: Wave reflection from breakwater. *Journal of Waterway, Port, Coastal, and Ocean Engineering*, **121**, 262–268, https://doi.org/10.1061/(ASCE)0733-950X(1995)121:5(262).

Elgar, S., T. H. C. Herbers, and R. T. Guza, 1994: Reflection of ocean surface gravity waves from a natural beach. *Journal of Physical Oceanography*, **24**, 1503–1511, https://doi.org/10.1175/1520-0485(1994)024<1503:ROOSGW>2.0.CO;2.

Elgar, S., B. Raubenheimer, and T. H. C. Herbers, 2003: Bragg reflection of ocean waves from sandbars. *Geophysical Research Letters*, **30**, 16–1–16–4, https://doi.org/https://doi.org/10.1029/2002GL016351.

Gerling, T. W., 1992: Partitioning sequences and arrays of directional ocean wave spectra into component wave systems. *Journal of Atmospheric and Oceanic Technology*, **9**, 444–458, https://doi.org/10.1175/1520-0426(1992)009<0444:PSAAOD>2.0.CO;2.

Gon, C. J., J. H. MacMahan, E. B. Thornton, and M. Denny, 2020: Wave dissipation by bottom friction on the inner shelf of a rocky shore. *Journal of Geophysical Research: Oceans*, **125**, e2019JC015 963, https://doi.org/https://doi.org/10.1029/2019JC015963.

Guillaume, A., 1990: Statistical tests for the comparison of surface gravity wave spectra with application to model validation. *Journal of Atmospheric and Oceanic Technology*, **7**, 551 – 567, https://doi.org/10.1175/1520-0426(1990)007<0551:STFTCO>2.0.CO;2.

Hashimoto, N., and K. Konbune, 1988: Directional spectrum estimation from a bayesian approach. *21st Coastal Engineering Conference*, Costa del Sol-Malaga, Spain, 62-76, https://doi.org/10.9753/icce.v21.4.

Hashimoto, N., T. Nagai, and T. Asai, 1994: Extension of the maximum entropy principle method for directional wave spectrum estimation. *24th Coastal Engineering Conference*, Kobe, Japan, 232-246, https://doi.org/10.1061/9780784400890.019.

Hasselmann, S., C. Brüning, K. Hasselmann, and P. Heimbach, 1996: An improved algorithm for the retrieval of ocean wave spectra from synthetic aperture radar image spectra. *Journal of Geophysical Research: Oceans*, **101**, 16 615–16 629, https://doi.org/https://doi.org/10.1029/96JC00798.

Henderson, S. M., R. T. Guza, S. Elgar, and T. H. C. Herbers, 2006: Refraction of surface gravity waves by shear waves. *Journal of Physical Oceanography*, **36**, 629–635, https://doi.org/10.1175/JPO2890.1.

Herbers, T. H., P. F. Jessen, T. T. Janssen, D. B. Colbert, and J. H. MacMahan, 2012: Observing ocean surface waves with gps-tracked buoys. *Journal of Atmospheric and Oceanic Technology*, **29**, 944–959, https://doi.org/10.1175/JTECH-D-11-00128.1.

Herbers, T. H., and S. J. Lentz, 2010: Observing directional properties of ocean swell with an acoustic doppler current profiler (adcp). *Journal of Atmospheric and Oceanic Technology*, **27**, 210–225, https://doi.org/10.1175/2009JTECHO681.1.

Herbers, T. H. C., S. Elgar, and R. T. Guza, 1999: Directional spreading of waves in the nearshore. *Journal of Geophysical Research: Oceans*, **104**, 7683–7693, https://doi.org/https://doi.org/10.1029/1998JC900092.

Herbers, T. H. C., R. L. Lowe, and R. T. Guza, 1991: Field verification of acoustic doppler surface gravity wave measurements. *Journal of Geophysical Research: Oceans*, **96**, 17 023–17 035, https://doi.org/https://doi.org/10.1029/91JC01326.

Huntley, D. A., S. David, and T. Rao, 1999: Use of collocated sensors to measure coastal wave reflection. *Journal of Waterway, Port, Coastal, and Ocean Engineering*, **125**, 46–52, https://doi.org/10.1061/(ASCE)0733-950X(1999)125:1(46).

Huntley, D. A., and M. A. Davidson, 1998: Estimating the directional spectrum of waves near a reflector. *Journal of Waterway, Port, Coastal, and Ocean Engineering*, **124**, 312–319, https://doi.org/10.1061/(ASCE)0733-950X(1998)124:6(312).

Kennedy, D. M., and J. G. Beban, 2005: Shore platform morphology on a rapidly uplifting coast, wellington, new zealand. *Earth Surface Processes and Landforms*, **30**, 823–832, https://doi.org/https://doi.org/10.1002/esp.1192.

Kuik, A. J., G. P. van Vledder, and L. H. Holthuijsen, 1988: A method for the routine analysis of pitch-and-roll buoy wave data. *Journal of Physical Oceanography*, **18**, 1020–1034, https://doi.org/10.1175/1520-0485(1988)018<1020:AMFTRA>2.0.CO;2.

Lancaster, O., R. Cossu, S. Boulay, S. Hunter, and T. E. Baldock, 2021: Comparative wave measurements at a wave energy site with a recently developed low-cost wave buoy (spotter), adcp, and pressure loggers. *Journal of Atmospheric and Oceanic Technology*, **38**, 1019–1033, https://doi.org/10.1175/JTECH-D-20-0168.1.

Lin, Z., T. A. Adcock, and M. L. McAllister, 2022: Estimating ocean wave directional spreading using wave following buoys: a comparison of experimental buoy and gauge data. *Journal of Ocean Engineering and Marine Energy*, **8**, 83–97, https://doi.org/10.1007/s40722-021-00218-7.

Longuet-Higgins, M. S., D. E. Cartwright, and N. D. Smith, 1961: Observations of the directional spectrum of sea waves using the motion of a floating buoy. *Proceedings of a Conference on Ocean Wave Spectra*, Easton, Maryland, The U.S. Naval Oceanographic Office and the Division of Earth Sciences, National Academy of Sciences National Research Council, 111-136.

MacMahan, J. H., A. J. H. M. Reniers, E. B. Thornton, and T. P. Stanton, 2004: Surf zone eddies coupled with rip current morphology. *Journal of Geophysical Research: Oceans*, **109**, https://doi.org/https://doi.org/10.1029/2003JC002083.

MacMahan, J. H., E. B. Thornton, A. J. H. M. Reniers, T. P. Stanton, and G. Symonds, 2008: Low-energy rip currents associated with small bathymetric variations. *Marine Geology*, **255**, 156–164, https://doi.org/https://doi.org/10.1016/j.margeo.2008.08.006.

Marshall, R. J., and W. J. Stephenson, 2011: The morphodynamics of shore platforms in a micro-tidal setting: Interactions between waves and morphology. *Marine Geology*, **288**, 18–31, https://doi.org/10.1016/J.MARGEO.2011.06.007.

Matsuba, Y., D. Roelvink, A. J. H. M. Reniers, D. P. Rijnsdorp, and T. Shimozono, 2022: Reconstruction of directional spectra of infragravity waves. *Journal of Geophysical Research: Oceans*, **127**, e2021JC018 273, https://doi.org/https://doi.org/10.1029/2021JC018273.

Miche, M., 1951: Le pouvoir réfléchissant des ouvrages maritimes exposés à l'action de la houle. *Annales de Ponts et Chaussées, 121 (285-319)*.

Monismith, S. G., J. S. Rogers, D. Koweek, and R. B. Dunbar, 2015: Frictional wave dissipation on a remarkably rough reef. *Geophysical Research Letters*, **42**, 4063–4071, https://doi.org/https://doi.org/10.1002/2015GL063804.

Poate, T., G. Masselink, M. J. Austin, M. Dickson, and R. McCall, 2018: The role of bed roughness in wave transformation across sloping rock shore platforms. *Journal of Geophysical Research: Earth Surface*, **123**, 97–123, https://doi.org/https://doi.org/10.1002/2017JF004277.

Raghukumar, K., G. Chang, F. Spada, C. Jones, T. Janssen, and A. Gans, 2019: Performance characteristics of "spotter," a newly developed real-time wave measurement buoy. *Journal of Atmospheric and Oceanic Technology*, **36**, 1127 – 1141, https://doi.org/10.1175/JTECH-D-18-0151.1.

Reniers, A. J. H. M., E. L. Gallagher, J. H. MacMahan, J. A. Brown, A. A. van Rooijen, J. S. M. van Thiel de Vries, and B. C. van Prooijen, 2013: Observations and modeling of steep-beach grain-size variability. *Journal of Geophysical Research: Oceans*, **118**, 577–591, https://doi.org/https://doi.org/10.1029/2012JC008073.

Shanks, A. L., J. MacMahan, S. G. Morgan, R. AJHM, M. Jarvis, J. Brown, A. Fujimura, and C. Griesemer, 2015: Transport of larvae and detritus across the surf zone of a steep reflective pocket beach. *Marine Ecology Progress Series*, **528**, 71–86.

Sunamura, T., 1992: *Geomorphology of rocky coasts*, Vol. 3. John Wiley Sons, pp 302.

Tatavarti, R. V. S. N., D. A. Huntley, and A. J. Bowen, 1988: Incoming and outgoing wave interactions on beaches. *21st Coastal Engineering Conference*, Costa del Sol-Malaga, Spain, 136-150, https://doi.org/10.1061/9780872626874.010.

Nortek, 2017: Signature operations v7. Nortek, 52 pp, https://www.nortekgroup.com/assets/software/N3015-002-SignatureOperations2505001000C.pdf.

OCM Partners, 2023: USGS Topobathy CoNED DEM: Northern California from 2010-06-15 to 2010-08-15. NOAA National Centers for Environmental Information, https://www.fisheries.noaa.gov/inport/item/62987.

Sofar Ocean, 2023: Spotter buoy by sofar. Sofar Ocean Technologies, https://www.sofarocean.com/products/spotter.

Walton, T. L., 1992: Wave reflection from natural beaches. *Ocean Engineering*, **19**, 239–258, https://doi.org/https://doi.org/10.1016/0029-8018(92)90027-2.

THIS PAGE INTENTIONALLY LEFT BLANK

Initial Distribution List

1. Defense Technical Information Center
   Ft. Belvoir, Virginia

2. Dudley Knox Library
   Naval Postgraduate School
   Monterey, California